Icarus 218 (2012) 707–722

Contents lists available at SciVerse ScienceDirect

Icarus

journal homepage: www.elsevier.com/locate/icarus

Titan global climate model: A new 3-dimensional version of the IPSL Titan GCM

Sébastien Lebonnois [a,*], Jérémie Burgalat [b], Pascal Rannou [b,c], Benjamin Charnay [a]

[a] Laboratoire de Météorologie Dynamique, IPSL, CNRS/UPMC, Box 99, F-75252 Paris Cedex 05, France
[b] GSMA, UMR CNRS 6089, Université de Reims Champagne-Ardenne, France
[c] LATMOS, IPSL, CNRS/UVSQ, Guyancourt, France

ARTICLE INFO

Article history:
Received 14 April 2011
Revised 17 November 2011
Accepted 25 November 2011
Available online 8 December 2011

Keywords:
Titan
Atmospheres, Dynamics

ABSTRACT

We have developed a new 3-dimensional climate model for Titan's atmosphere, using the physics of the IPSL Titan 2-dimensional climate model with the current version of the LMDZ General Circulation Model dynamical core. Microphysics and photochemistry are still computed as zonal averages. This GCM covers altitudes from surface to 500 km altitude, with barotropic waves now being resolved and the diurnal cycle included. The boundary layer scheme has been changed, yielding a strong improvement in the tropospheric zonal wind profile modeled at Huygens descent position and season. The potential temperature profile is fairly consistent with Huygens observations in the lowest 10 km. The latitudinal profile of the near-surface temperature is close to observed values. The minimum of zonal wind observed by the Huygens probe just above the tropopause is also present in these simulations, and its origin is discussed by comparing solar heating and dynamical transport of energy. The stratospheric temperature and wind fields are consistent with our previous works. Compared to observations, the zonal wind peak is too weak (around 120 m/s) and too low (around 200 km). The temperature structures appear to be compressed in altitude, and depart strongly from observations in the upper stratosphere. These discrepancies are correlated, and most probably related to the altitude of the haze production. The model produces a detached haze layer located more than 150 km lower than observed by the Cassini instruments. This low production altitude is due to the current position of the GCM upper boundary. However, the temporal behaviour of the detached haze layer in the model may explain the seasonal differences observed between Cassini and Voyager 1. The waves present in the GCM are analyzed, together with their respective roles in the angular momentum budget. Though the role of the mean meridional circulation in momentum transport is similar to previous work, and the transport by barotropic waves is clearly seen in the stratosphere, a significant part of the transport at high latitudes is done all year long through low-frequency tropospheric waves that may be baroclinic waves.

1. Introduction

The Cassini mission to Saturn and Titan continues to send many data, that greatly improves our knowledge of Titan's atmosphere and surface. As the years go by, the season in the Saturnian system has been moving from northern winter at Cassini's arrival and Huygens mission ($L_s \sim 300°$) into northern spring at present. This allows the retrieval of seasonal effects in the distribution of temperatures, tropospheric clouds, stratospheric haze and chemical compounds.

The dominant features of the temperature and dynamics of Titan's atmosphere observed recently with the CIRS instrument on board the Cassini mission have been reviewed in Flasar and Achterberg (2009). In the temperature structure at this season, a latitudinal contrast is observed in the stratosphere, with the equator slightly warmer than the southern (summer) polar region, and the northern (winter) polar region colder by 20 K. The warmest region of the stratopause is located over the winter polar region (where the stratopause occurs at higher altitudes than at low-latitudes, 0.01 hPa versus 0.1 hPa), indicative of a subsidence over the winter pole. From the temperature structure, the cyclostrophic winds are derived and show a strong jet in the winter hemisphere, with stratospheric zonal winds up to 190 m/s (Achterberg et al., 2008b). Another feature deduced from the CIRS dataset is the fact that the polar vortices appear to be tilted by a few degrees relative to the spin axis of Titan (Achterberg et al., 2008a).

The CIRS spectra have also determined the stratospheric distributions of photochemical compounds (Teanby et al., 2009b; Coustenis et al., 2010). Latitudinal profiles in the stratosphere are retrieved from nadir observations (e.g. Coustenis et al., 2007; Teanby et al., 2006, 2009a), as well as vertical profiles at several latitudes from limb observations (e.g. Teanby et al., 2007; Vinatier et al., 2007, 2010). These observations have determined the

* Corresponding author.
E-mail address: Sebastien.Lebonnois@lmd.jussieu.fr (S. Lebonnois).

0019-1035/$ - see front matter © 2011 Elsevier Inc. All rights reserved.
doi:10.1016/j.icarus.2011.11.032

latitude–pressure distribution of many chemical compounds in Titan's troposphere, confirming the enrichment in the northern (winter) polar region compared to other latitudes, already observed at a different season (just after northern spring equinox) with the IRIS instrument on board Voyager 1 (Coustenis and Bézard, 1995). This characteristic feature is consistent with the subsidence within the winter polar vortex, as discussed by Teanby et al. (2008a). Comparing IRIS/Voyager 1 and CIRS/Cassini datasets enables to investigate seasonal variations in the stratospheric composition (Teanby et al., 2008b; Coustenis et al., 2010).

On January 14th, 2005, the Huygens probe landed on Titan's surface. During its descent, the data acquired by the onboard instruments determined vertical profiles of atmospheric temperature, pressure (Fulchignoni et al., 2005), wind speed (Bird et al., 2005; Folkner et al., 2006), haze (Tomasko et al., 2005) and composition (Niemann et al., 2005) at 10°S latitude. Properties of the boundary layer have also been inferred from Huygens data (Tokano et al., 2006). Huygens results are reviewed by Lebreton et al. (2009).

Stratospheric winds and composition have also been observed from Earth using different techniques: with the Infrared Space Observatory (Coustenis et al., 2003), with submillimeter radiotelescopes (Marten et al., 2002; Moreno et al., 2005), with high-resolution infrared heterodyne interferometry (Kostiuk et al., 2001, 2005, 2006), with Doppler shift in reflected solar lines (Luz et al., 2005), and also through analysis of Titan stellar occultations (Hubbard et al., 1993; Bouchez, 2004; Sicardy et al., 2006). These Earth-based observations, though providing less spatial resolution, allow for a larger sampling of the seasonal variations.

Starting with Del Genio et al. (1993) and Hourdin et al. (1995), several Titan atmosphere General Circulation Models have been developed, based on different Earth GCMs: the Köln model (Tokano et al., 1999), which has been used for many studies on Titan's troposphere (for a review, see Tokano, 2009); a 2-dimensional model mainly used to study the tropospheric methane cycle (Mitchell et al., 2006); a non-hydrostatic GCM developed in Russia (Mingalev et al., 2006); a Titan version of the PlanetWRF GCM (Richardson et al., 2007); a Titan version of the CAM model (Friedson et al., 2009). Most of these models have difficulties reproducing the high zonal winds observed in Titan's stratosphere. A recent version of the TitanWRF model (Newman et al., 2011) obtains strong superrotation comparable to observations, and the authors demonstrate how sensitive it is to assumed values of horizontal dissipation.

Development of the LMD Titan atmospheric model started in early 1990s, based on the GCM dynamical core developed for the Earth's atmosphere. Hourdin et al. (1995) managed to spin up the atmosphere of Titan from rest up to superrotation with zonal winds comparable to observed values. The vertical range of this GCM was from the surface up to 250 km. Radiative transfer was computed using a prescribed vertical profile of haze and gases (inheritated from McKay et al. (1989)) horizontally uniform on the planet. In order to include coupling with haze, Rannou et al. (2002, 2004) developed a 2-dimensional axisymmetric (latitude–altitude) version of the model that demonstrated strong interaction between haze distribution and dynamics. This model covered altitudes up to ~500 km and it was able to interpret many features of the haze layer, in particular the detached haze observed at 350 km altitude at the time of Voyager 1. This IPSL 2-dimensional climate model (2D-CM) was further developed to include the photochemical model of Lebonnois et al. (2001), and the effects of the coupling between chemical composition and dynamics were studied (Lebonnois et al., 2003; Hourdin et al., 2004). A recent comparison of the CIRS/Cassini results with the latest version of the IPSL 2D-CM was published by Crespin et al. (2008). The model reproduces the thermal structure observed in the troposphere and stratosphere, the abundance and vertical profiles of most chemical compounds in the stratosphere, and their enrichment in the winter polar region. A reference simulation may be found on the web (Rannou et al., 2005), and a review of the interactions between haze, dynamics and composition may be found in Lebonnois et al. (2009).

This 2-dimensional climate model uses a specific parametrization to take into account the horizontal mixing by barotropic waves, which were obtained in the 3-dimensional GCM of Hourdin et al. (1995) but could not be present in the 2-dimensional reduction of the model. This parametrization was developed by Luz and Hourdin (2003) and Luz et al. (2003). It uses diagnosed barotropic instabilities to evaluate the horizontal mixing coefficient associated with the corresponding waves. This mixing is part of the angular momentum budget and plays a key role in the superrotation, but no ad hoc tuning was done to get the successful simulation of observed features detailed previously.

However, the best way to confirm the conclusions from the 2-dimensional climate model is to take advantage of the increase in computing power available to develop a new version of the 3-dimensional GCM. This model is now operational, simulations have been run and analysis is presented below. The model is detailed in Section 2. In Section 3, the results for stratospheric circulation are compared to observations and to the previous 2D-CM results. Some aspects of the tropospheric circulation are described in Section 4.

2. Description of the GCM

2.1. Dynamical core

The LMDZ4 dynamical core, currently used for the Earth (Hourdin et al., 2006) and for Venus (Lebonnois et al., 2010) has been adapted for Titan's atmosphere. This dynamical core is based on a finite-difference discretization scheme that conserves both potential enstrophy for barotropic nondivergent flows, and total angular momentum for axisymmetric flows. A longitudinal filter is applied in polar regions (poleward of 60° latitude) to limit the effective resolution to that at 60°. The model is currently used with a resolution of 32 longitudes by 48 latitudes (11.25° × 3.75°), but a resolution of 64 × 48 has also been tested to estimate the impact of the longitudinal resolution. This increased resolution did not significantly affect the results discussed in this paper. The dynamical time-step is 3 min (reduced to 1.5 min for the higher longitudinal resolution). The model uses a leapfrog time integration scheme, with a periodic predictor–corrector time-step. Horizontal dissipation is done similarly to Earth and Venus, using an iterated laplacian with a time constant of 2×10^5 s below roughly 400 hPa (25 km altitude), 1×10^5 s between 400 hPa and 4 hPa (25 and 130 km), and 2×10^4 s above, with smoothed transitions over a few layers.

The vertical grid of the model is based on hybrid coordinates, though for the moment no topography is included, so model levels basically coincide with constant-pressure levels, with a surface pressure of 1.467 bar (Fulchignoni et al., 2005). We use 55 vertical levels, from the surface to roughly 550 km altitude. This grid is close to the one used in the 2-dimensional studies, listed in Table 1 of Rannou et al. (2005). Note that the altitudes listed in that table were computed based on a constant gravity g. When taking into account the thickness of the atmosphere compared to Titan's radius and the corresponding variation of g with altitude, as it is the case in this GCM, the real altitudes of the uppermost levels are greater than those indicated in Rannou et al. (2005). Pressures and altitudes of layer mid-points are displayed in Table 1. In the top three layers of the GCM, a sponge layer is included, with Rayleigh friction damping horizontal winds to zero. Time constants are 2.5×10^4 s (0.3 Earth days) for the top layer, then 5×10^4 and 1×10^5 s for

Table 1
Globally averaged pressure and altitude for the 55 vertical layers of the GCM.

Layer	Pressure (Pa)	Altitude (km)	Layer	Pressure (Pa)	Altitude (km)
1	1.464×10^5	0.035	29	4.75×10^2	124
2	1.456×10^5	0.147	30	3.54×10^2	134
3	1.439×10^5	0.39	31	2.64×10^2	145
4	1.401×10^5	0.93	32	1.97×10^2	156
5	1.329×10^5	1.98	33	1.47×10^2	167
6	1.216×10^5	3.74	34	1.10×10^2	179
7	1.080×10^5	6.05	35	82	191
8	9.48×10^4	8.55	36	61	203
9	8.21×10^4	11.2	37	45	215
10	6.97×10^4	14.3	38	34	228
11	5.80×10^4	17.5	39	25	241
12	4.75×10^4	21.0	40	19	255
13	3.83×10^4	24.6	41	14	268
14	3.05×10^4	28.4	42	10	282
15	2.40×10^4	32.3	43	7.8	297
16	1.87×10^4	36.3	44	5.7	313
17	1.44×10^4	40.4	45	4.2	330
18	1.10×10^4	44.7	46	3.1	348
19	8.39×10^3	49.2	47	2.2	367
20	6.34×10^3	53.9	48	1.6	387
21	4.77×10^3	58.9	49	1.2	405
22	3.58×10^3	64.6	50	1.0	418
23	2.69×10^3	71.2	51	0.74	437
24	2.02×10^3	78.6	52	0.46	467
25	1.52×10^3	86.7	53	0.29	497
26	1.14×10^3	95.3	54	0.20	522
27	8.50×10^2	104	55	0.14	546
28	6.36×10^2	114			

the two layers below. These values are identical to those used in the IPSL 2D-CM.

Though gravitational tides have recently been added to our model (Charnay and Lebonnois, 2011), the simulations presented here do not include them. The impact on the results discussed here is small.

2.2. Physical parametrizations

The physical parametrizations have been mostly taken from the IPSL 2D-CM (see Rannou et al., 2004, 2005; Crespin et al., 2008). We will discuss here the most important differences.

Though the radiative transfer is similar, the 3-dimensional geometry allows inclusion of the diurnal cycle. The radiative transfer is computed frequently, 10 times per Titan day in these simulations. Though a higher frequency has been used for a study of the diurnal cycle near the surface (Charnay and Lebonnois, 2011), the influence of this parameter on the results discussed in this paper is negligeable. Even without any diurnal cycle, results are close to those presented here.

For the boundary layer scheme, we use a "Mellor and Yamada" parameterization (Mellor and Yamada, 1982), taken from the Earth version of the LMD GCM. This parameterization is fully described in the Appendix B of Hourdin et al. (2002). The surface drag coefficient is $C_d = (0.4/\ln(1 + z_1/z_0))^2$, where z_1 is the altitude of the center of the first layer (equal to 10 m), and z_0 is the roughness coefficient, taken equal to 0.5 cm, as estimated from Huygens data by Tokano et al. (2006). The value of C_d is then equal to the value deduced from Huygens data, 2.8×10^{-3} (Tokano et al., 2006).

The soil model used here for thermal conduction in the soil is the same 11-layer model as for the other GCMs developed at LMD (Hourdin et al., 1993). The model depends on the thermal inertia of the surface, chosen here to be $I = 2000\ \mathrm{J\ m^{-2}\ s^{-0.5}\ K^{-1}}$. A simulation was also performed with $I = 340\ \mathrm{J\ m^{-2}\ s^{-0.5}\ K^{-1}}$. The influence on the results discussed in this paper is small. However, thermal inertia affects the temporal evolution of the surface temperature, as well as its latitudinal profile at a given season. Other surface parameters include the albedo (0.15) and the emissivity (0.95).

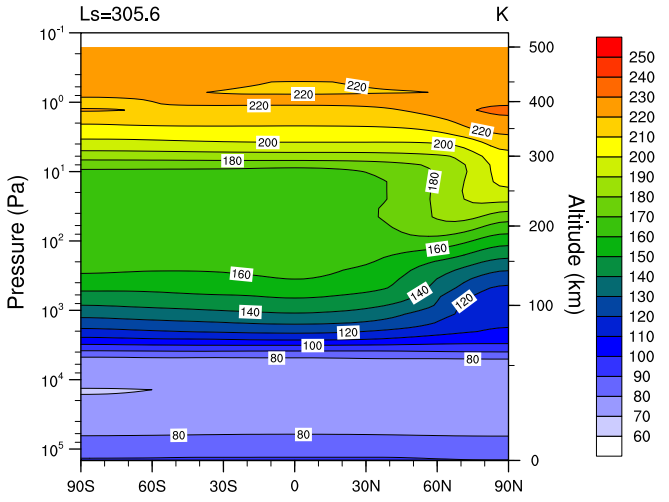

Fig. 1. Modeled latitude-pressure distribution of the zonally averaged temperature after the Cassini arrival ($L_s \sim 305°$). The altitude scale on the right axis is approximate.

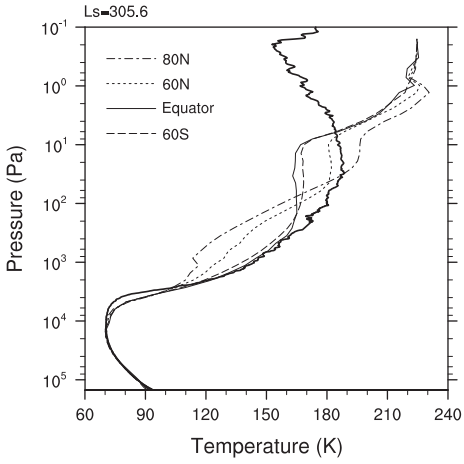

Fig. 2. Modeled vertical profiles of temperature at latitudes 60S, equator, 60°N and 80°N ($L_s \sim 305°$). The HASI/Huygens vertical profile (10S) is plotted for comparison (bold line).

2.3. Haze microphysics and photochemistry

Due to computational cost, it is difficult to compute photochemical and haze microphysical tendencies at every longitude. However, the relative variation of the haze layer in the longitudinal direction is extremely weak. No variation have been reported in observations at the scale of the model grid (500 km). Therefore, zonally averaging the microphysics is not anticipated to produce significant loss of information in the model, though this approximation precludes study of longitudinal variations of atmospheric composition related to the diurnal variability. We adopted the following technique: at each time-step, the 3-dimensional fields of microphysical and photochemical tracers are zonally averaged, before computing the tendencies as diurnal averages in the same microphysical and photochemical modules as in the IPSL 2D-CM (Rannou et al., 2004; Crespin et al., 2008). The tendencies are then converted back to 3-dimensional fields proportionally to the corre-

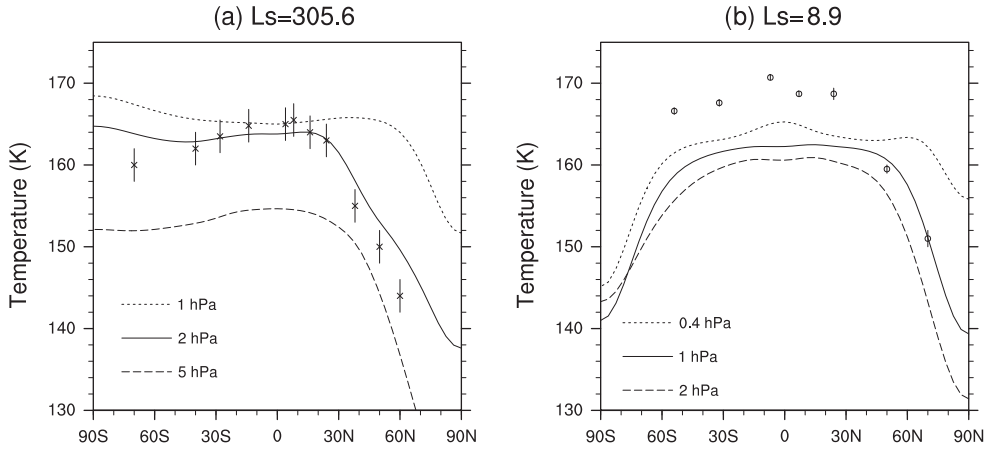

Fig. 3. Latitudinal profiles of modeled temperatures: (a) at 1, 2 and 5 hPa, L_s 305° to compare to CIRS/Cassini data at 1.8 hPa (crosses with error bars, Flasar et al., 2005) and (b) at 0.4, 1 and 2 hPa, L_s 9° to compare to IRIS/Voyager 1 data at 1 hPa (circles with error bars, Coustenis and Bézard, 1995).

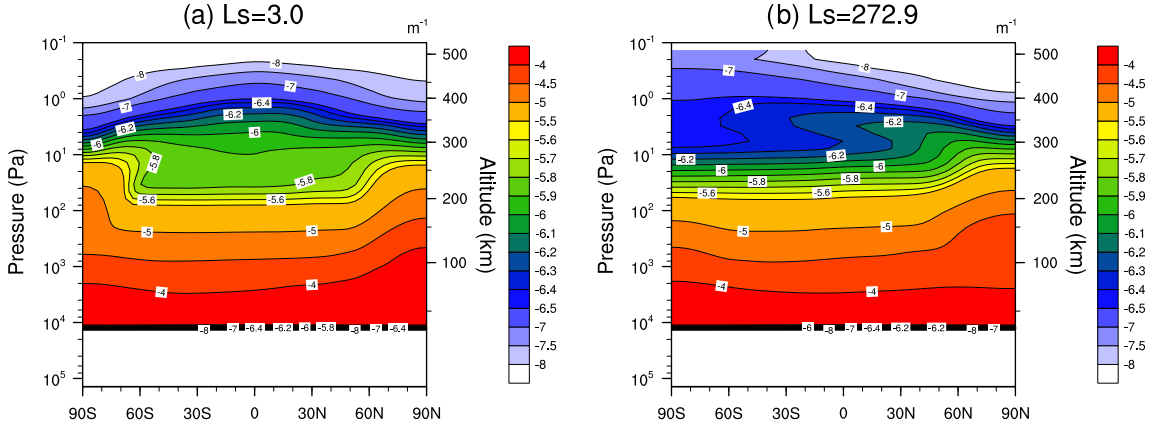

Fig. 4. Modeled latitude-pressure distribution of the zonally averaged opacity field at 700 nm, for (a) northern spring equinox and (b) northern winter solstice. The altitude scale on the right axis is approximate.

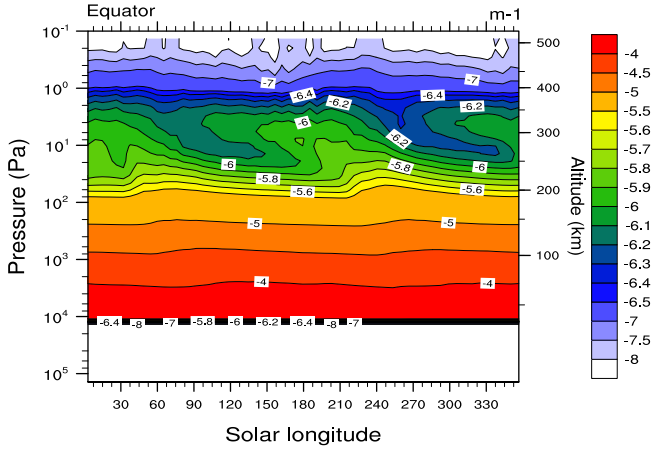

Fig. 5. Annual variations of the modeled vertical profile of the zonally averaged equatorial opacity at 700 nm. The altitude scale on the right axis is approximate.

sponding tracer field. The total mass is conserved in this scheme. Only the microphysical and photochemical modules are affected by this zonal average; haze and chemical compounds are advected by the full 3-dimensional circulation. Photochemistry is computed only once per Titan day (as in 2D), while the microphysics is computed 200 times per day.

No cloud microphysics was included in this GCM configuration. This work is underway for methane, ethane, and acetylene (based on Rannou et al. (2006)) and will be the subject of a future publication. Inclusion of a cloud model would affect the results in the troposphere, but essentially at second order. From preliminary results including the clouds (out of the scope of this paper), the methane cycle does not alter significantly the results described here.

As a starting point, we used the haze and composition distributions taken from Crespin et al. (2008), at northern spring equinox ($L_s = 0°$). However, haze opacity has been artificially reduced everywhere at the beginning of the simulation, to let the 3-dimensional GCM reach its own equilibrium regime. Production has been maintained at the value used in the 2D simulations, 1.0×10^{-12} kg m^{-2} s^{-1}, peaking at 1 Pa (roughly 400 km altitude).

2.4. Initial conditions and simulation parameters

The initial fields were all taken from the two-dimensional simulations described in Crespin et al. (2008) at northern spring equinox, including all components of the wind, and the temperature. These 2-dimensional fields were used as uniform in longitude. This means the model is not started from rest. The surface pressure was adjusted to the Huygens value, 1.467 bar (Fulchignoni et al., 2005).

The simulations were run for 12 Titan years. During the first year, the total angular momentum decreased by 40%, due to the

significant adjustment of the wind profile in the troposphere. After that, its relative variations are limited to roughly 1.5% the second year, 0.8% the third year, and less than 0.5% the following years. The stability from 1 year to the other is good, though longer simulations may still yield some small variations. Test variations of input parameters have some impact on the total angular momentum (up to a few percent) depending on the influence of the modified parameter on tropospheric wind speeds. Output is averaged over 1 Titan "week" of 11 Titan days, giving 61 weeks/Titan year (i.e. 673 Titan days, the latest 2 weeks having 12 days instead of 11).

A test simulation started from rest has been run with decoupled haze, i.e. a fixed vertical profile of haze opacity, uniform in the horizontal. This haze distribution was taken from an averaged distribution obtained with the 2-dimensional model. It run for 15 Titan years, which may not be long enough (Newman et al., 2011), with the evolution of the total angular momentum around 0.7% per year after this time. The superrotation was much smaller than in the simulation started from the 2-dimensional simulations, with maximum zonal wind speed limited to ~40 m/s. Further analysis will be done in future work, in particular the influence of the altitude distribution of the haze (strongly affecting the temperature structure), as well as the horizontal dissipation scheme, as Newman et al. (2011) showed the extremely large influence this parameter may have on the spin-up. This is also a question under study in Venus atmosphere modeling (Lebonnois et al., 2010, 2011).

3. Results in the stratosphere

The modeled fields are compared here to available observations. Emphasis is also given to differences with the ISPL 2D-CM results. Discussions concerning this model refer to the work of Crespin et al. (2008) (hereafter C08).

3.1. Temperature structure

The zonally averaged temperature structure in northern winter ($L_s \sim 300°$) is shown in Figs. 1, 2 and 3a. As in the IPSL 2D-CM simulations, the temperature vertical profiles below 2 hPa (160 km) compare quite well with observations (see Figs. 1–3, C08). However, above this level, modeled stratospheric temperatures are significantly colder than observations. In addition, the absence of a stratopause and mesosphere is still present, pointing to the same radiative transfer problem as discussed in C08. The latitudinal features are similar to observations (Achterberg et al., 2008b) and to the 2D simulations, but the polar contrasts and structures in the winter (northern) stratosphere appear lowered in altitude in the $10–10^{-2}$ hPa region compared to observations. This difference may be related to the haze distribution over the winter polar region and to the misrepresentation of the atmospheric structure above 0.3 hPa (250 km). As discussed in C08, one reason for this misrepresentation is the modeled altitude of the detached haze layer (as shown in the next section), which is much too low compared to observations due to the model limitations in the altitude domain.

The thermal structure after spring equinox, compared to IRIS/Voyager 1 data, is not as accurate as in previous versions of our model, as shown in Fig. 3b (to be compared to Fig. 14, Rannou et al., 2004). This disagreement with observations must be related to the haze distribution and associated circulation in this GCM which are not fully satisfying, as discussed in more detail in the following sections. The temperature contrasts are smaller than in the 2D simulations, especially around equinox, with consequences for wind speeds.

3.2. Haze distribution

The formation of the detached haze layer has been discussed in connection with the meridional circulation and production region by Rannou et al. (2002, 2004). The mechanism is the following. In the production zone (around 1 Pa/400 km altitude), the particles grow and are blown towards the winter pole by the mean meridional circulation. In the winter hemisphere, they settle down, leave the production region and grow as fractal aggregates. Though they accumulate dominantly over the winter polar region, they are mixed in the stratosphere by the stratospheric dynamics. In the summer hemisphere, ascending motions help maintain a population of particles in the detached haze layer, corresponding to the top of the dominant meridional circulation, that includes both small spheres from the formation region and fractal aggregates from the main haze layer.

In the 3-dimensional simulations presented here, the resulting detached layer is located around 6–3 Pa (300–350 km altitude) most of the time, slightly lower than in the 2D-CM simulations (C08). This is consistent with smaller latitudinal temperature contrasts and weaker winds (see next section). The meridional shape of the haze opacity at 700 nm is shown in Fig. 4 for northern spring

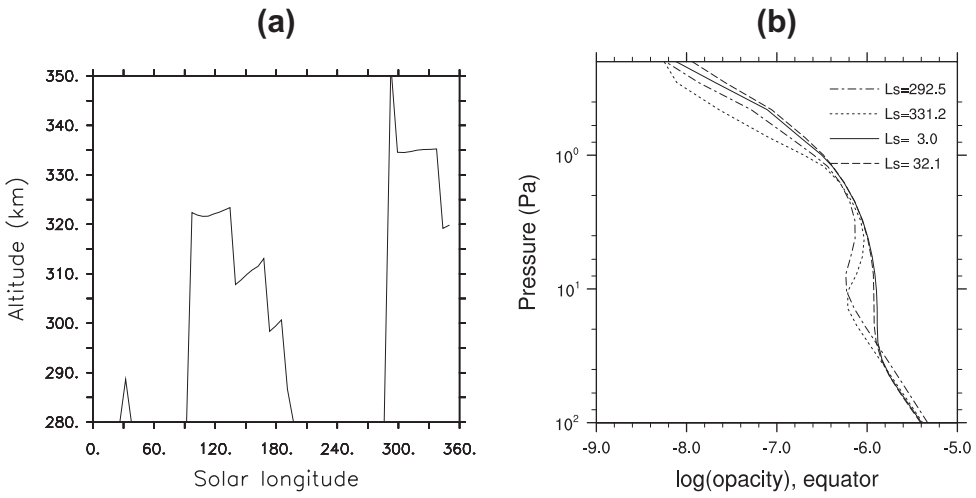

Fig. 6. (a) Approximate altitude of the maximum opacity at 700 nm in the detached haze layer as a function of the solar longitude. (b) Vertical profile of the zonally averaged equatorial opacity, during northern winter and beginning of spring.

equinox and northern winter solstice. This shape is very close to the results obtained with the 2D-CM. The position of the detached haze layer is closely related to the temperature increase above the 10 Pa level, which also affects the meridional circulation in a feedback loop. This increase of temperature right at the detached haze layer position is also seen in the Huygens observations (Fulchignoni et al., 2005).

In Fig. 5, the evolution of the vertical profile of the opacity is shown at the equator during 1 Titan year (year 12 of our simulation). The detached haze layer disappears around $L_s \sim 30°$ and $\sim 210°$, before building up again just after the solstices. As illustrated in Fig. 6a, it is mostly located in a constant altitude range (310–340 km in this simulation). The evolution of this haze layer during northern winter and spring is plotted in Fig. 6b. It illustrates the fact that quickly after equinox, the detached haze layer moves downward before disappearing. Qualitatively, this might explain the difference in altitude of the detached haze layer between the Cassini mission (roughly 510 km, $L_s \sim 300°$ to 360°) and the Voyager 1 observation (around 350 km, $L_s = 9°$), despite a wrong altitude. The timing of this descent of the detached haze layer corresponds to the position of the ascending motions around the 10 Pa level during this season. The ascending branch joining the two Hadley cells is located over the summer polar region, then shifts equatorward to reach the equator at equinox. It gradually

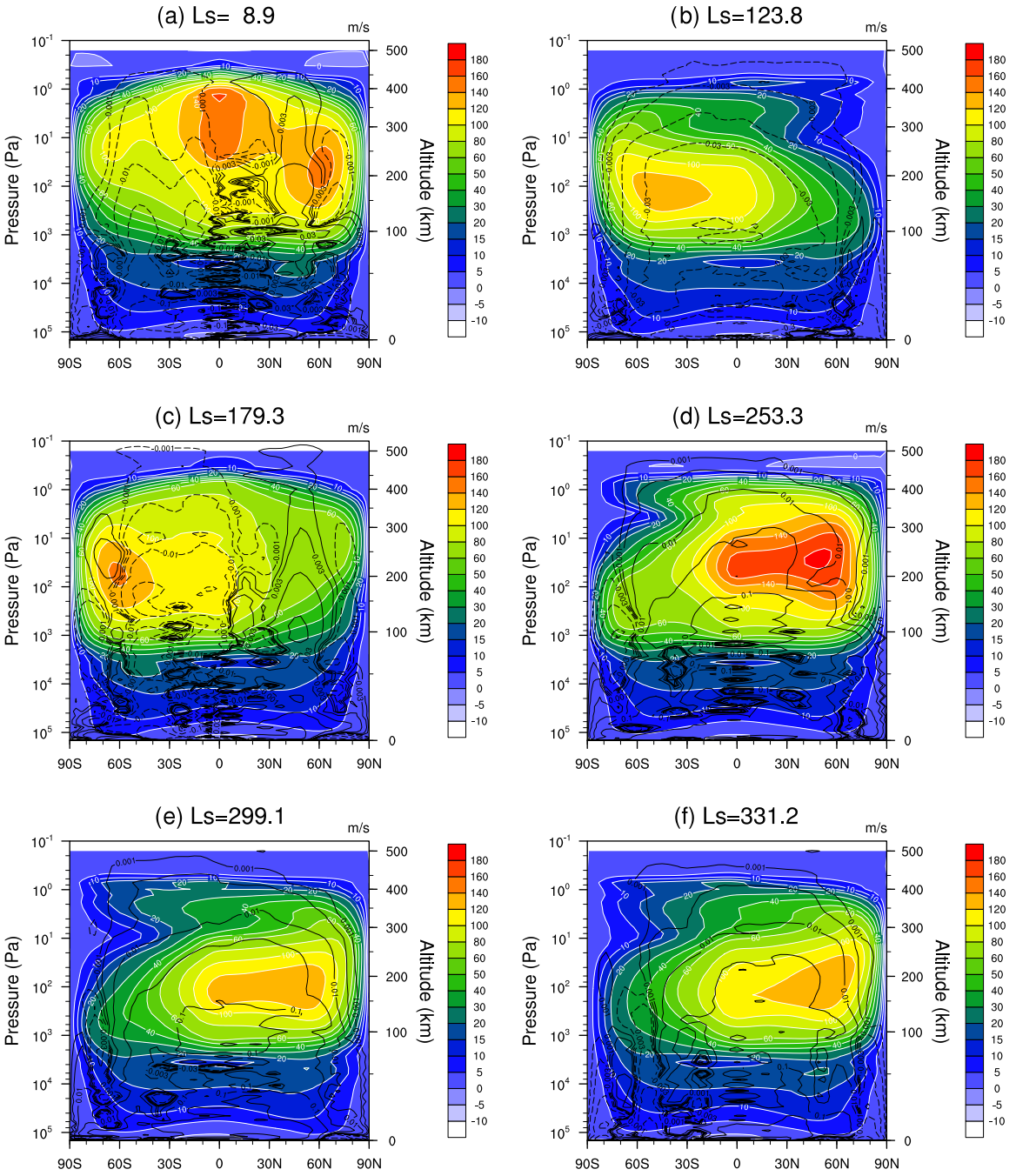

Fig. 7. Mean zonal wind field (colors) obtained with the simulations during year 6 at several seasons: (a) $L_s = 9°$, Voyager 1; (b) $L_s = 124°$, close to the period of the 1989 stellar occultation; (c) $L_s = 180°$, northern autumn equinox. (d) $L_s = 255°$, close to the period of the 2001 stellar occultation; (e) $L_s = 300°$, beginning of Cassini observations and close to the 2003 stellar occultation; (f) $L_s = 330°$, during Cassini observations. The zonally averaged meridional stream function is shown as black contours (solid line is clockwise rotation, dashed line is anti-clockwise, unit is 10^9 kg/s). The altitude scale on the right axis is approximate.

shifts further toward higher latitudes, reaching the future summer polar region after $L_s = 30°$. During this shift, the detached haze layer sinks down into the main haze layer over both poles. At the equator, it also goes down, and even disappears everywhere well into the equinox season, before building up again over the spring polar regions when the solstice approaches. This behavior of the detached haze layer is model dependent, of course, but it helps explain why this layer was observed lower after equinox (Voyager 1) than during the solstice season (Cassini). Since the Cassini mission is monitoring the detached haze layer during equinox and the following season, it should provide extremely valuable informations on the variations of the detached haze layer altitude during this crucial period.

The discrepancy between the modeled and observed positions of the detached haze layer must certainly have an impact on the position and amplitude of the zonal wind jet. We need to extend the model vertically to improve this aspect of the simulations. However, this is not straightforward to do, because of the atmospheric thickness (already far beyond the acceptable limit for the shallow water approximation ($Z_C \ll R_T$) where Z_C is the vertical extension of the model and R_T is the radius of Titan) and because of the radiative transfer (HCN needs to be taken into account in a realistic way, as demonstrated in Lebonnois et al. (2003)).

3.3. Zonal winds

The zonal wind field is presented at several seasons in Fig. 7, together with the meridional stream function. For $L_s = 300–330°$, this circulation may be compared to the thermal winds retrieved from CIRS/Cassini data (Achterberg et al., 2008b). The jet is both too low and weaker compared to the retrieved thermal wind and to the 2D modeled zonal wind (C08), which is consistent with the disagreement obtained in the thermal structure at the same season (Fig. 1).

The seasonal variations of the superrotation have been observed at least partially thanks to Earth-based observations, see Table 1 in Kostiuk et al. (2010) and Fig. 13 in Sicardy et al. (2006). The modeled seasonal variations of the zonal winds at altitudes around 145–200 km (300–60 hPa) and 250–310 km (20–6 hPa) are shown in Fig. 8. Though the higher region should be considered for comparison to most observations, the lower position of the modeled jet at the Cassini season indicates that the lower region of the model may be more relevant for comparison.

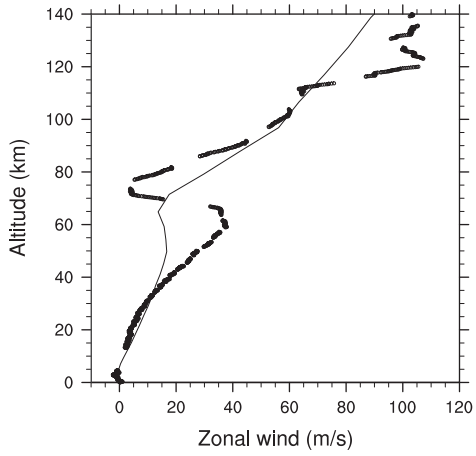

Fig. 9. Vertical profile of the zonal wind at 10°S, at a season close to the Huygens probe landing. Huygens observed profile is indicated with black dots.

The amplitude of the zonal winds are under-estimated in the model, for all solar longitudes. During solstice seasons, modeled winds are above 120 m/s around 200 km altitude (where the peak is located), while observations indicate a peak around 180–220 m/s: (Hubbard et al., 1993), $L_s = 128°$; (Sicardy et al., 2006; Kostiuk et al., 2005), $L_s = 290°$; (Achterberg et al., 2008b), $L_s = 300–330°$. Right before northern summer solstice ($L_s = 255°$), Bouchez (2004) have retrieved a northern peak up to 220 m/s, but also indication of winds that are still around 160–200 m/s in the southern hemisphere. For this season, the model predicts the highest zonal winds in the autumn hemisphere, but the winds in the spring hemisphere have decreased around mid-season, before the observations reported in Bouchez (2004). This disagreement may be related to the seasonal variations in the position of the jet and to the amplitude question, as there are hints in Figs. 7d and 8a that strong winds are still present in mid-southern latitudes at this season below 200 km altitude, though decreasing rapidly with time. Around equinox ($L_s = 160–190°$), (Kostiuk et al., 2001) reported high zonal wind speeds ($u = 210 \pm 150$ m/s). Again, modeled values are lower than observed, but the winds obtained in the GCM at this season are slightly higher than the peak of the solstice season, consistent with the observed value compared to Cassini season retrievals.

As shown in Fig. 9, the wind profile in the troposphere and lower stratosphere at the Huygens probe landing site position and sea-

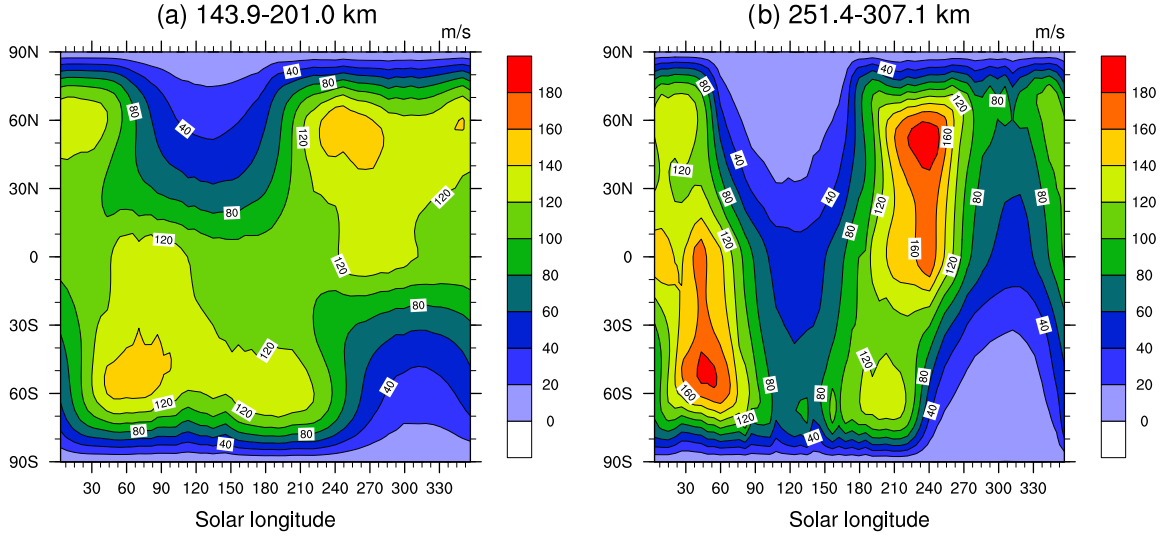

Fig. 8. Seasonal variations of the latitudinal profile of the mean zonal wind averaged in altitude regions (a) 145–200 km and (b) 250–300 km.

son is in reasonable agreement with the observed profile. The shape of the tropospheric zonal wind is significantly improved compared to the 2D simulations shown in C08. A minimum of zonal wind, as observed by Huygens around 20–40 hPa (60–75 km altitude), is obtained in the model though at lower altitude (35–75 hPa; 50–65 km), as it was already the case in the 2D simulations (C08). This local minimum is not as deep as in the Huygens data.

For the radiative relaxation time, this region is a transition (Flasar et al., 1981). Above 10 hPa, it is less than half a Titan year, so the seasonal variations of the solar forcing drives significant seasonal variations in the temperature. Below 50 hPa, the radiative relaxation time is more than 2 Titan years, so the temperature structure is more sensitive to the annual mean of solar forcing.

This region corresponds also to the maximum of stability, with the strongest temperature increase with altitude, just above the tropopause region. There, the meridional winds reverse compared to dominant winds above, inducing a partial division in the Hadley-type cells (both for the pole-to-pole cell present most of the year and for the two equator-to-pole cells present around equinoxes).

As shown in Hourdin et al. (1995), the temperature is very uniform in latitude in this region, both in radiative–convective simulations and in GCM simulations. In these first GCM simulations of the circulation in Titan's atmosphere, a minimum of zonal wind was already present in the 30–40 hPa region. In the simulations presented here, the latitudinal contrasts of temperature are also very small, and they are even reversed at low-latitudes, with the equator temperature being colder than mid-latitude temperatures, at all seasons. This reversal ΔT (over a latitude region $\Delta\phi$) is correlated with the decrease of zonal wind Δu with altitude (Δz). They are linked through the thermal wind equation:

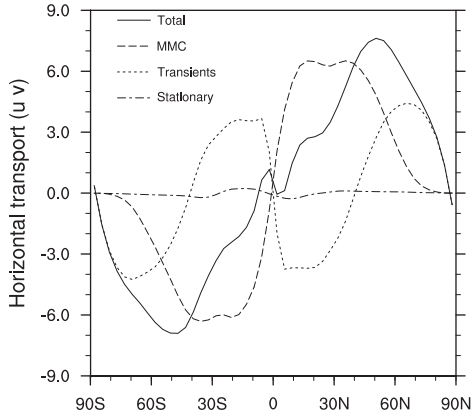

Fig. 11. Annual average of the latitudinal transport of angular momentum by mean meridional circulation (MMC, dashed line), transient waves (dotted line) and stationary waves (dash-dotted line). Total is shown in solid line. Unit is 10^3 m^3/s^2, positive values are northward.

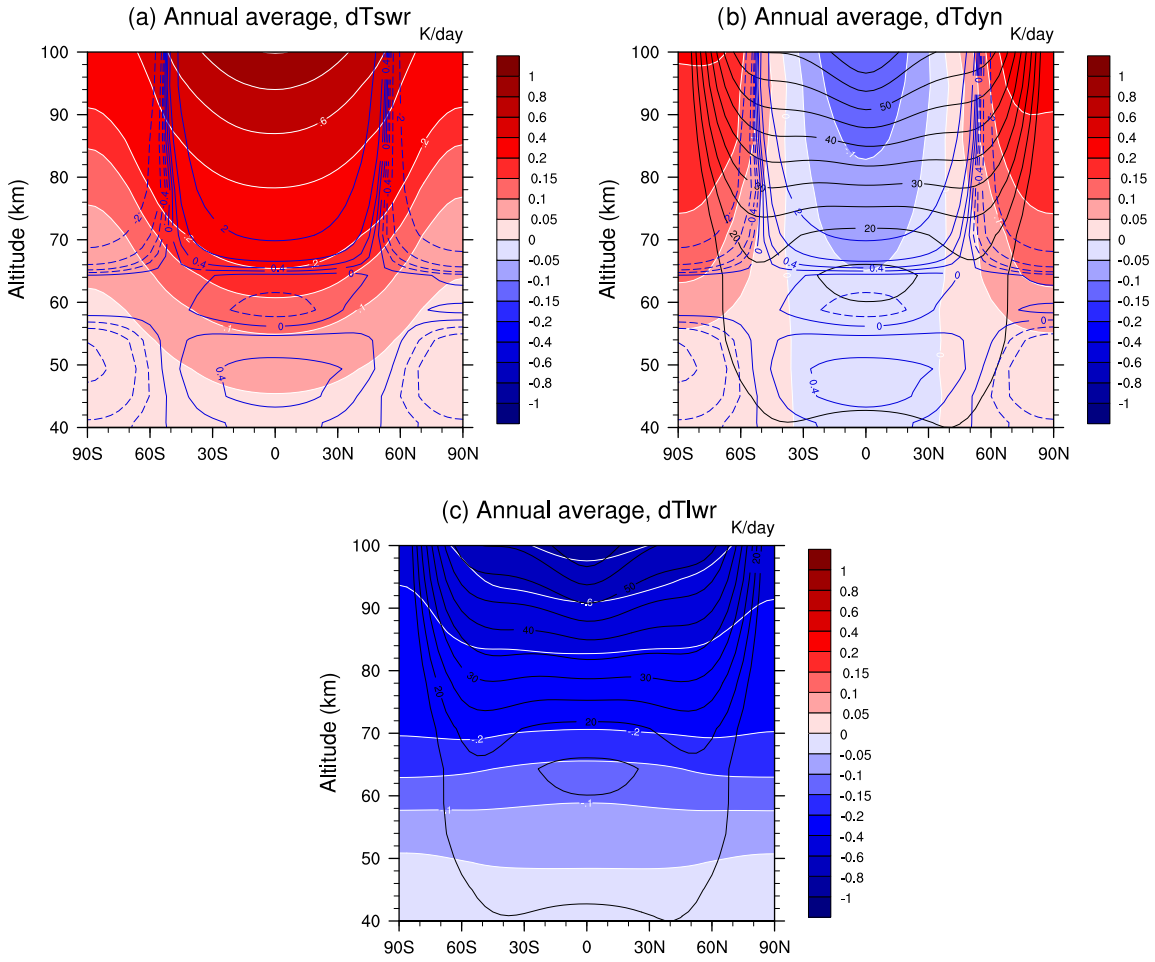

Fig. 10. Annual average of (a) the solar heating rates, (b) the dynamical heating rates and (c) the infrared cooling rates in the lower stratosphere. Units are K/Titan day. The blue contours (a and b) show the difference between the annual average of the temperature and its latitudinal mean (latitudinal contrast, in K). The black contours (b and c) indicate the annual average of the zonal wind (in m/s). (For interpretation of the references to color in this figure legend, the reader is referred to the web version of this article.)

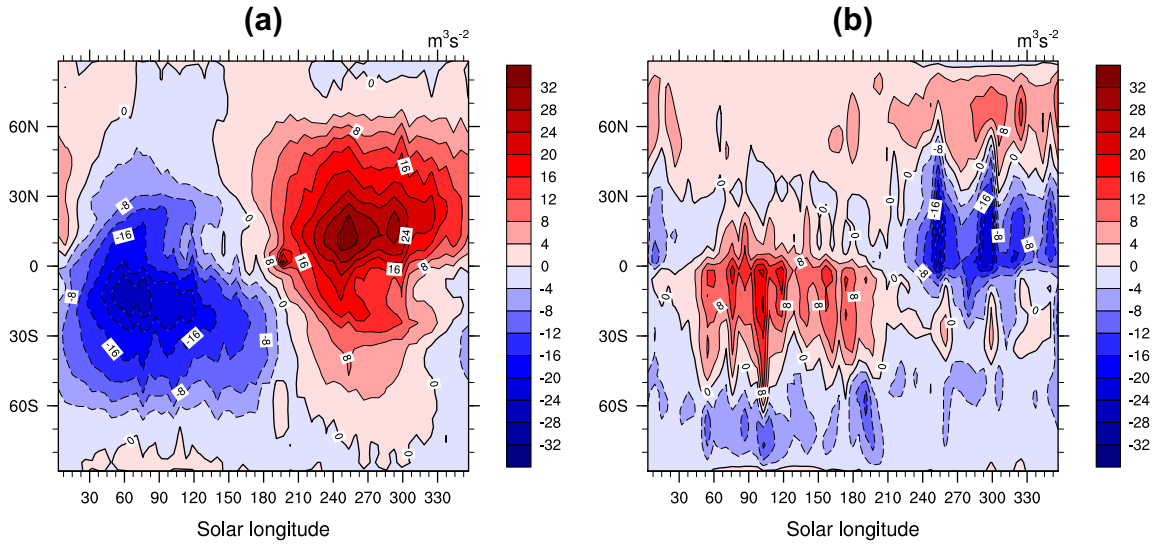

Fig. 12. Seasonal variations of the latitudinal transport of angular momentum by (a) mean meridional circulation and (b) transient waves. Unit is 10^3 m^3/s^2, positive values are northward.

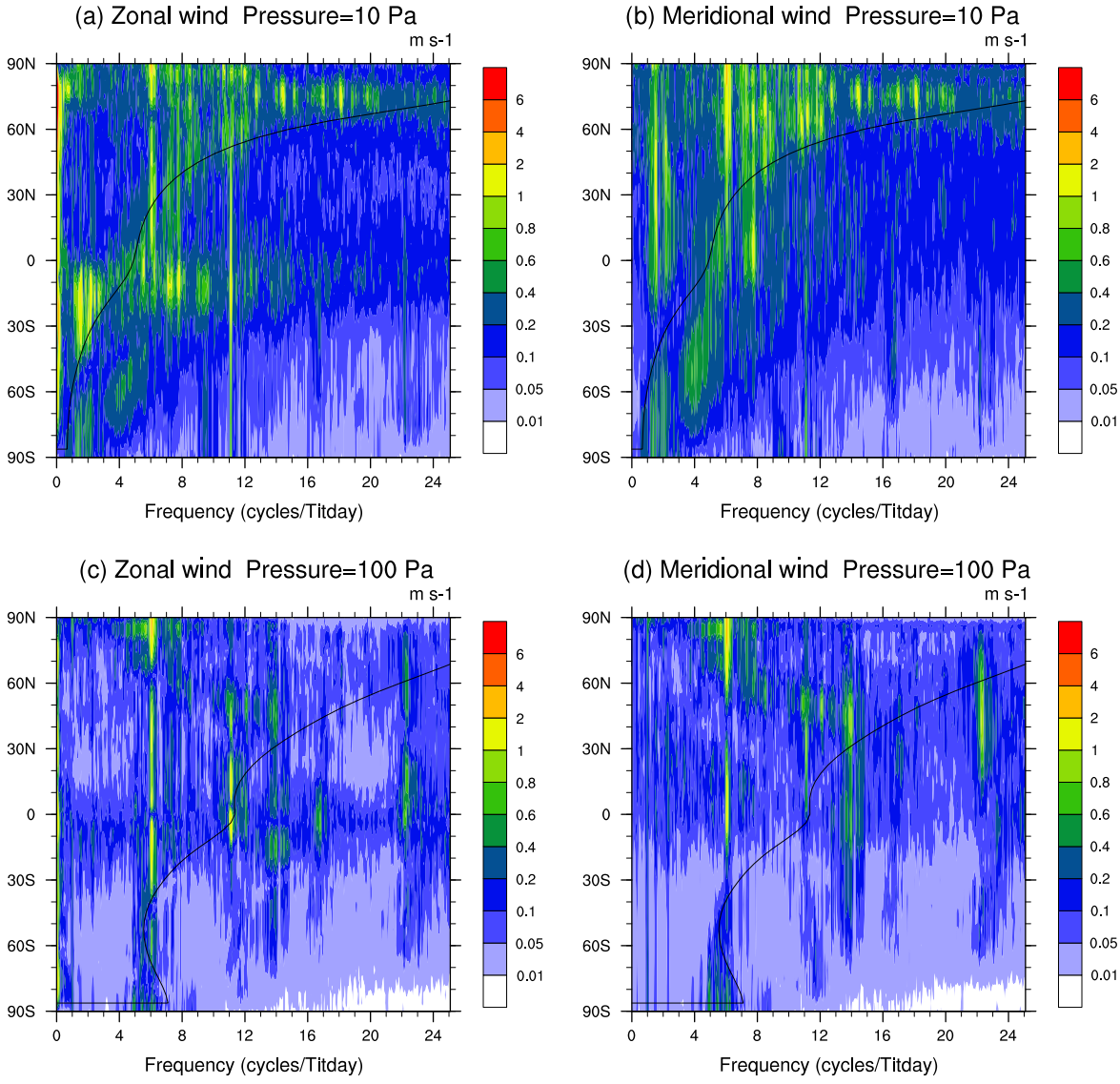

Fig. 13. Zonally averaged amplitude frequency spectrum for the zonal and meridional wind fields as a function of latitude, at pressure levels of 10 and 100 Pa. Chosen season is $L_s = 295°$. The solid curve is the mean zonal rotation speed of the flow (same unit as the frequency).

$$\frac{\partial}{\partial z}\left(2\Omega u\sin\phi+\frac{u^2\tan\phi}{a}\right)=-\frac{g}{Ta}\frac{\partial T}{\partial\phi}, \tag{1}$$

where $a = 2.575\times10^6$ m is the radius of Titan, $\Omega = 4.56\times10^{-6}$ s^{-1} is the rotation rate of Titan, ϕ is the latitude, $g = 1.35$ m s^{-2} is the gravity, z (m) is the altitude, T (K) is the temperature and u (m s^{-1}) is the zonal wind speed. This equation is presented here in the thin atmosphere approximation. It is further approximated to link $\frac{\Delta T}{\Delta\phi}$ to $\frac{\Delta u}{\Delta z}$:

$$\frac{-\Delta u}{\Delta z}\left(2\Omega\sin\phi+\frac{2u\tan\phi}{a}\right)=\frac{g}{Ta}\frac{\Delta T}{\Delta\phi}. \tag{2}$$

In the GCM simulation presented in this work, the following values are estimated: $u\sim16$ m s^{-1}, $T\sim90$ K, $\phi\sim\pi/12$ (averaged value for the region between the equator and 30°), $\Delta u\sim-4$ m s^{-1}, $\Delta z\sim1\times10^4$ m, $\Delta T\sim0.2$ K and $\Delta\phi\sim\pi/6$. The first term evaluates to

$$\frac{-\Delta u}{\Delta z}\left(2\Omega\sin\phi+\frac{2u\tan\phi}{a}\right)=2.3\times10^{-9}\ \text{s}^{-2}.$$

The second term evaluates to

$$\frac{g}{Ta}\frac{\Delta T}{\Delta\phi}=2.2\times10^{-9}\ \text{s}^{-2}.$$

Given the approximations done, the agreement is quite good, confirming that the zonal wind and temperature fields are related through the thermal wind equation. If we apply the same calculation to the observed profile, with $u\sim20$ m s^{-1} (averaged value in the decrease region), $T\sim90$ K, $\Delta u\sim-40$ m s^{-1}, $\Delta z\sim1.5\times10^4$ m, and $\phi\sim\sin\phi\sim\tan\phi\sim\frac{\Delta\phi}{2}$, ΔT may be evaluated as

$$\Delta T=\frac{-\Delta u}{\Delta z}\left(\Omega+\frac{u}{a}\right)\frac{Ta}{g}(\Delta\phi)^2, \tag{3}$$

i.e.

$$\Delta T=5.65\times(\Delta\phi)^2.$$

If the meridional temperature inversion is located between equator and mid-latitudes ($\Delta\phi$ between 30 and 45°), this relation should yield a latitudinal contrast in temperature around 1.5–3.5 K. This may be possible to observe with the Cassini radio-occultation data (Schinder et al., 2011).

Fig. 10 shows the annual average of the solar heating rates, heating due to dynamics, and cooling by infrared radiation (these three tendencies are balanced). Between the tropopause and 70 km, the solar heating at equator is compensated by the cooling due to ascending motions, resulting in a slightly lower cooling needed around equator than at mid-latitudes. Therefore, our model suggests that this relative distribution of solar heating versus dynamical tendencies forces a local minimum of temperature in this region. Through the thermal wind equation, this local minimum induces a decrease in zonal wind with altitude, therefore driving the local minimum in zonal winds.

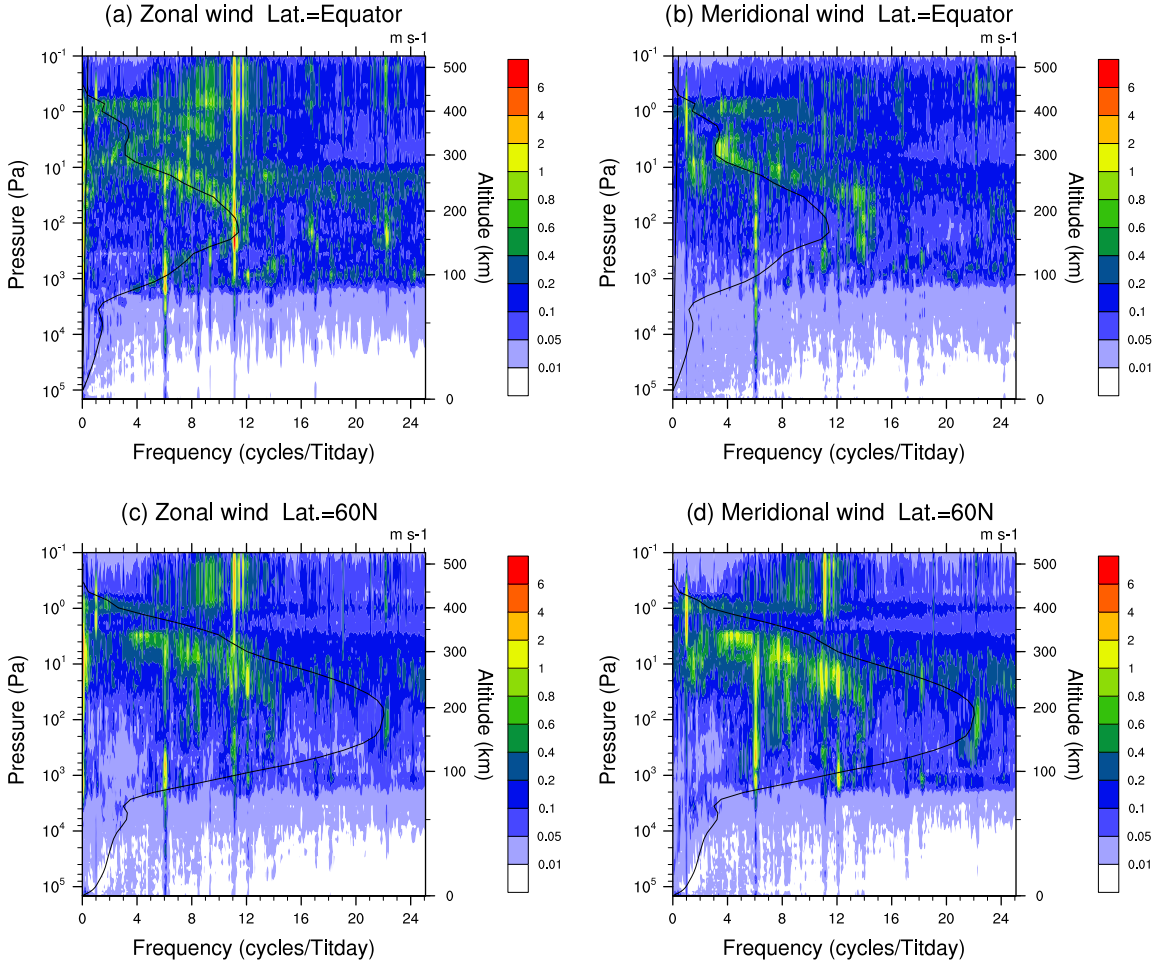

Fig. 14. Zonally averaged amplitude frequency spectrum for the zonal and meridional wind fields as a function of pressure, at equator and 60°N. Chosen season is $L_s = 295°$. The solid curve is the mean zonal rotation speed of the flow (same unit as the frequency). The altitude scale on the right axis is approximate.

3.4. Transport of angular momentum and waves

Averaged over 1 Titan year, the transport of angular momentum is quite similar to previous models (such as Hourdin et al., 1995). Here, the angular momentum transport is computed for each latitude ϕ as the integral over longitude λ and pressure p of the quantity $vua\cos\phi dm$, where dm is the element of mass ($dm = a^2\cos\phi d\phi\, d\lambda dp/g$), normalized by the mass:

$$\frac{\int vua\cos\phi dm}{\int dm} \quad \text{(expressed in m}^3/\text{s}^2\text{)}.$$

As shown in Fig. 11, the overall poleward transport of angular momentum by the mean meridional circulation (MMC) is partially compensated through transport by waves in the low- to mid-latitudes. Poleward of roughly 40°, angular momentum is transported toward poles both by transient waves and by the mean meridional circulation. The total poleward transport is balanced by exchanges of angular momentum between the surface and the atmosphere. The zonally and annually averaged zonal wind at the surface is negative below 30° latitude (transferring momentum from the surface into the atmosphere) and positive above (giving back momentum to the surface), as shown in Fig. 7. Fig. 12 shows the seasonal variations of the transport by the MMC and waves. The evolution of the MMC transport is consistent with the seasonal variations of the Hadley cells. The transport by transient waves follows a more complex pattern: at mid- to high-latitudes, the transport is continuously poleward, while between 40°N and 40°S, it is directed towards the spring/summer pole, stronger in the autumn/winter hemisphere where it counteracts the transport by the MMC, and reversing a third of season after the equinox. Significant variability is apparent in this horizontal transport by transients. This is consistent with the results of Newman et al. (2011), who find that stratospheric waves transporting angular momentum are particularly active during some episodes in the fall and winter seasons.

To analyze the waves present in our simulation, high-frequency output was recorded for 16 Titan days, 50 points per day, at $L_s \sim 295°$ where strong wave activity is visible. The eddy components of u and v at a given point in the atmosphere ($u'(t)$ and $v'(t)$) were computed as the difference between the fields $u(t)$ and $v(t)$ and their time average at this point. For each point in the atmosphere, a fast fourier transform was then performed on $u'(t)$ and $v'(t)$ after multiplication by a triangle function to limit the impact of the time window. The distribution of waves is illustrated in Fig. 13 at fixed pressures (10 and 100 Pa), and in Fig. 14 at fixed latitudes (equator and 60°N).

The most visible groups of waves in the u' fields are located around frequencies of ~6 cycles/Titan day (thereafter f_1) and ~11 cycles/Titan day (thereafter f_2), though above 100 Pa, the waves are more widely distributed in frequency. For v', the f_1 wave is the most visible feature. The amplitudes of u' and v' around these two frequencies are shown in the meridional plane in Fig. 15. Most activity is located in the 10^3–10 Pa pressure range, where the zonal wind jet is present, and at latitudes from 30°S to the northern (winter) pole, with u' peaking near the equator while v' is peaking in mid-latitudes. The latitudinal gradient of the absolute vorticity

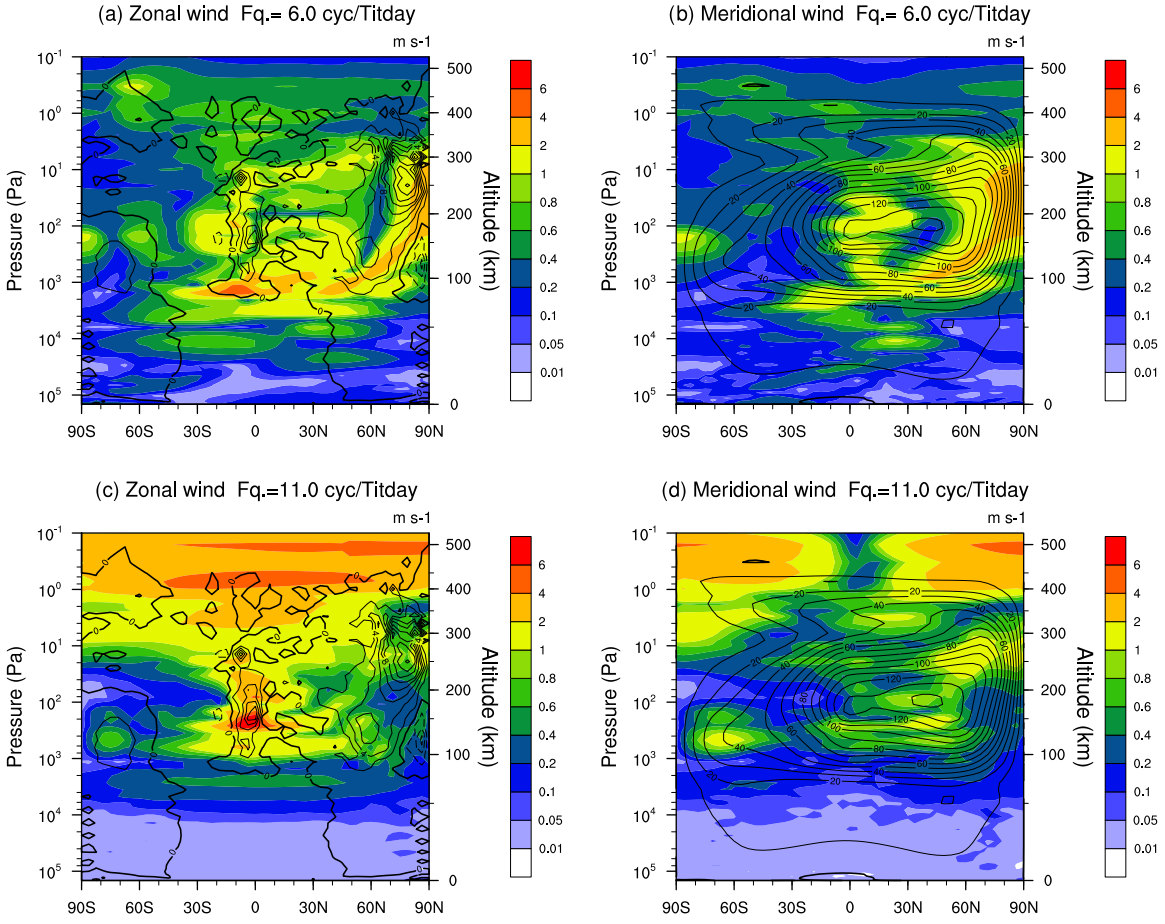

Fig. 15. Latitude–altitude distribution of the maximum amplitude of the transients in the frequency ranges 5–7 cycles/Titan day (f_1) and 10–12 cycles/Titan day (f_2) at $L_s = 295°$. (a and c) Amplitude on zonal wind, the solid contours are the latitudinal gradient of the absolute vorticity (in 10^{-11} m^{-1}s^{-1}). (b and d) Amplitude on meridional wind, the solid contours are the mean zonal wind field (in m/s).

$$\frac{\partial \overline{q}}{\partial y} = \frac{\partial}{a\partial\phi}\left(2\Omega \sin\phi - \frac{\partial \overline{u}}{a\partial\phi}\right) \quad (4)$$

(where $\overline{q}$ is the zonal average of q, the absolute vorticity) is used as a criterion for barotropic instabilities (Rayleigh-Kuo criterion, Kuo, 1949; Vallis, 2006): it must change sign in the region of instability. Fig. 15 confirms that the region where the waves are the most active is also a region where $\frac{\partial \overline{q}}{\partial y}$ is low and often changes sign. Therefore it is probable that these waves are barotropic in nature. Fig. 15 recalls work by Luz and Hourdin (2003) and Luz et al. (2003) (e.g. Fig. 15 of Luz et al. (2003)) in which the latitudinal gradient of potential vorticity was used to parameterize the eddy momentum transport in the IPSL 2D-CM. This confirms that instabilities in the 2D-CM and 3D GCM have similar distributions (and similar consequences in terms of angular momentum transport). The distribution of the f_1 wave shows a significant activity on the poleward side of the jet, compared to f_2.

To better investigate the role of each wave in the transport of angular momentum in this simulation, the transients have been separated into three frequency regions, using filters applied on the spectra: waves with frequencies lower than 4 cycles/Titan day (f_0), waves with frequencies between 4 and 8 cycles/Titan day (i.e. mainly f_1), and waves with larger frequencies (i.e. mainly f_2). Instantaneous horizontal field snapshots of filtered u' are plotted in Fig. 16. The chosen pressures correspond to regions of high amplitudes for each of these waves: around 200 Pa for f_2, around 10^3 Pa for f_1, and very close to the surface for f_0 (1.3×10^5 Pa). The stratospheric waves have wavenumber 1, while the f_0 tropospheric wave has higher wavenumbers. All these waves are eastward propagating. The dominant f_0 wave seen at southern mid-latitudes in Fig. 16a has a very low-frequency, around 0.2 cycles/Titan day. The stratospheric waves present very similar characteristics to the waves displayed in Newman et al. (2011), which had frequencies from around 5 cycles/Titan day during spin-up to around 16 cycles/Titan day at the end of their simulation.

In the regions where the f_0 wave is active, the zonal wind u is steadily increasing with altitude. Here, close to the surface, the dynamical regime is more baroclinic. A criterion similar to the Rayleigh-Kuo criterion for barotropic instabilities may be used to see whether baroclinic instabilities can grow: the latitudinal gradient of the absolute vorticity $\frac{\partial \overline{q}}{\partial y}$ must change sign in the vertical direction (Holton, 1992; Vallis, 2006). This is visible in the structures present in the troposphere in Fig. 15, close to the surface and close to the pole. This reinforces the hypothesis that the tropospheric f_0 waves are baroclinic in nature. Note that baroclinic instabilities were seen at high latitudes in simulations of superrotating atmospheres done by Mitchell and Vallis (2010), for intermediate thermal Rossby numbers. Near-surface waves have also recently been analyzed in a tropospheric Titan GCM simulation (Mitchell et al., 2011), in which they are connected to the precipitation patterns observed near equinox (Turtle et al., 2011). Mitchell et al. (2011) obtained mainly two wave modes, equatorial Kelvin waves and mid-latitude waves propagating westward, confined near the surface and presenting similarities with the waves we obtain here (though the f_0 waves presented in Fig. 16a are slowly propagating eastward, not westward).

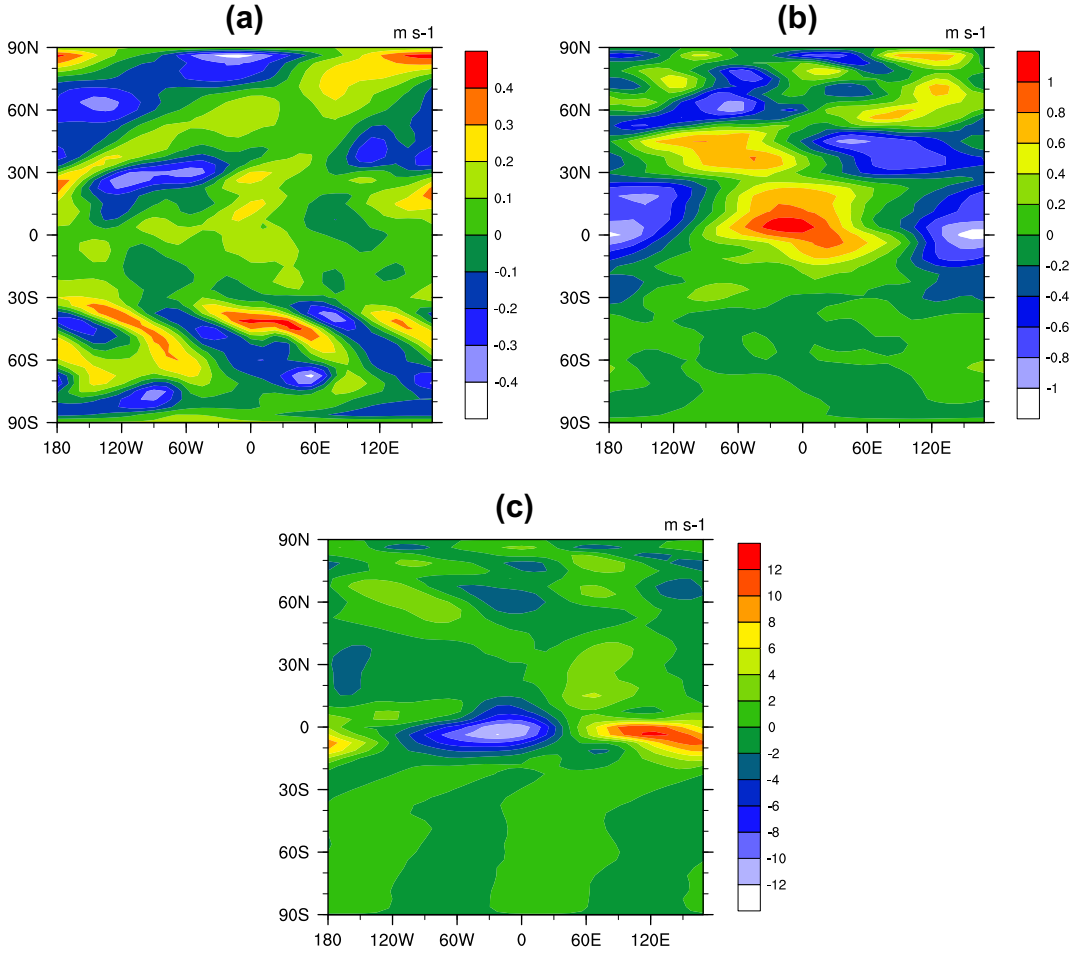

Fig. 16. Snapshots of the horizontal field of filtered perturbations on the zonal wind, at $L_s = 295°$. (a) $u'(f_0)$ in the lower troposphere, at 1.3×10^5 Pa; (b) $u'(f_1)$ in the stratosphere, at 10^3 Pa; (c) $u'(f_2)$ in the stratosphere, at 200 Pa.

The transport of angular momentum by each family of waves is computed using the filtered u' and v', and presented in Fig. 17, where it is split between upper atmosphere, stratosphere and troposphere. This transport is composed of two main components. The stratospheric waves (both f_1 and f_2 equally) transport a significant amount of angular momentum in the direction opposing the mean meridional circulation, especially during the solstice season. This transport also appears at low- to mid-latitudes in Figs. 11 and 12b. However, another component of the transport appears in Fig. 17: this is done by the low-frequency waves in the troposphere, at mid-to high-latitudes, despite their very low amplitude. This transport is directed towards the pole and is present even in periods of low barotropic wave activity. This component explains most of the transport seen poleward of 40° latitude in Figs. 11 and 12b.

To verify whether the high-latitude tropospheric component was related to the solar thermal tide, we have run a 1-year simulation without the diurnal cycle. During this year, the transport of angular momentum is not much affected; the same two components are found in the transport by waves, and the circulation is very similar to the nominal simulation with a diurnal cycle. This result is consistent with the small impact of the diurnal cycle obtained in Hourdin et al. (1995) and confirms that the high-latitude tropospheric transport in our simulations is not related to the solar thermal tide.

4. Results in the troposphere

The annual cycles of temperature at the surface and at the tropopause are shown in Fig. 18. The surface temperature is roughly 1 K below the value observed by Huygens (93.65 K, Fulchignoni et al., 2005), and the latitudinal contrast between winter polar regions and equator (around 2 K), as well as between summer polar regions and equator (around 0.6 K) are both under-estimated compared to the values retrieved by Jennings et al. (2009) (respectively 3 K and 2 K). The contrasts seen after northern spring equinox (1.5–2 K, almost symmetric) are consistent with IRIS/Voyager 1 observations. The modeled temperature at tropopause is very close to the Huygens observed value (70.4 K, Fulchignoni et al., 2005) and does not vary appreciably with either latitude or season. When the surface thermal inertia is reduced to $I = 340$ J m^{-2} s$^{-0.5}$ K^{-1}, the temporal variations of both surface and tropopause temperatures are slightly enhanced, and the temporal evolution of the surface maximum temperature is modified, with the maximum at $L_s \sim 300°$ displaced towards southern mid-latitudes.

The vertical profile of potential temperature at the Huygens landing site (Tokano et al., 2006, Fig. 2) shows an increase of roughly 5 K in the last 10 km, with a well-mixed boundary layer confined to 300 m above the surface. Shoulders in the profile are also seen around 800 m and 3 km altitude. A 2–3 km boundary layer is also consistent with dune spacing, as shown in Lorenz

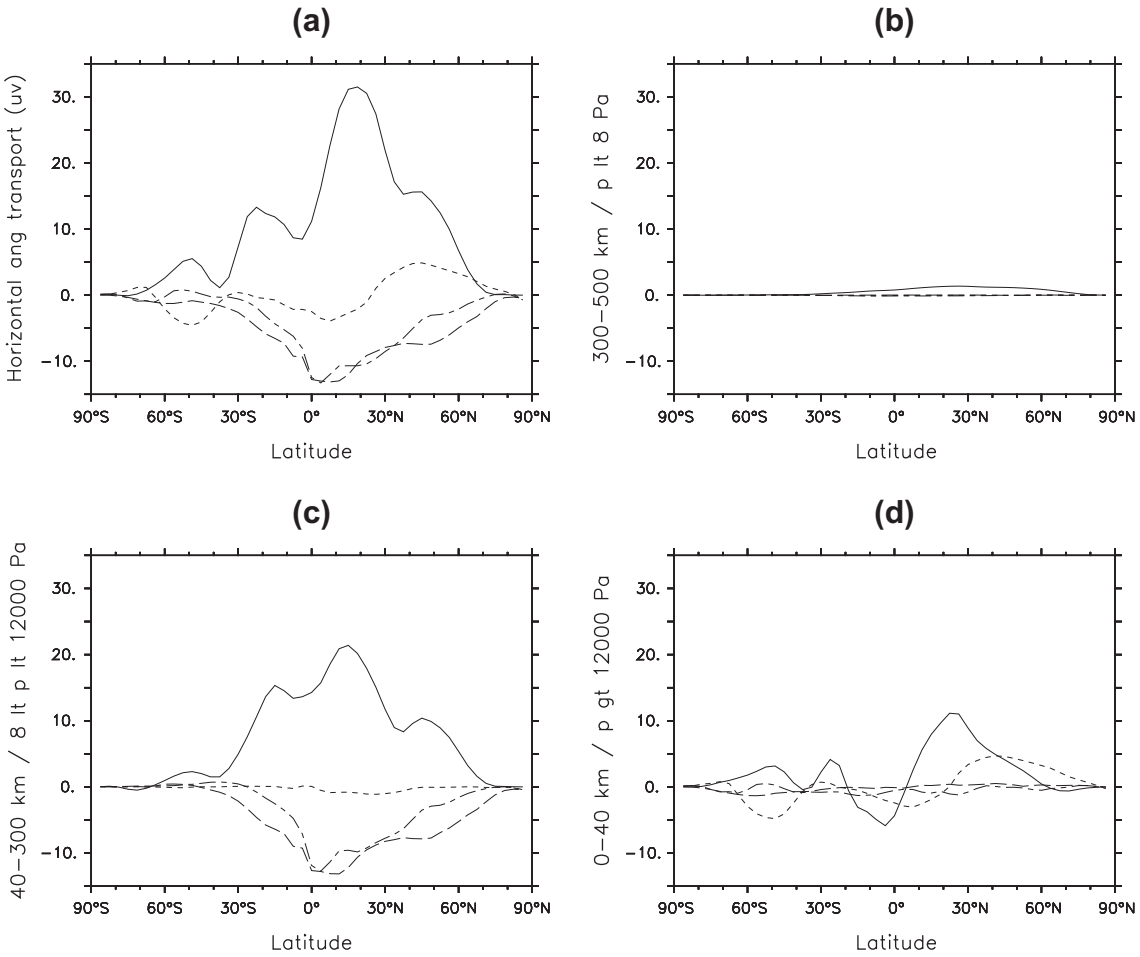

Fig. 17. Latitudinal transport of angular momentum in the simulation at $L_s = 295°$, for mean meridional circulation (solid lines), low-frequency transients (0–4 cycles/Titan day, dotted lines), transients with frequencies between 4 and 8 cycle/Titan day (i.e. mainly f_1, dashed lines) and high-frequency transients (above 8 cycle/Titan day, i.e. mainly f_2, dash-dotted lines). In panel (a), the relative angular momentum latitudinal transport is integrated for the entire column at each latitude, and is divided by the total mass of the column. In the other panels, it is integrated only for a fraction of the column, but it is still divided by the total mass of the entire column, so that the three plots add to give plot (a). Unit is 10^3 m^3/s^2, positive values are northward.

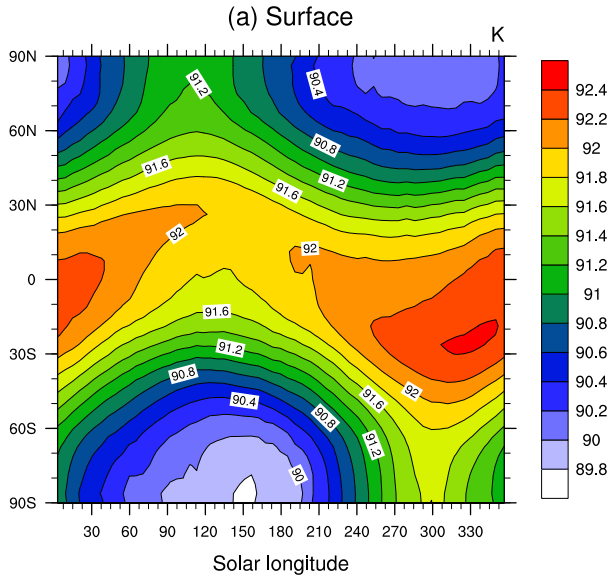

Fig. 18. Annual variations of the zonally averaged latitudinal temperature profile at (a) surface and (b) tropopause (roughly 40 km altitude).

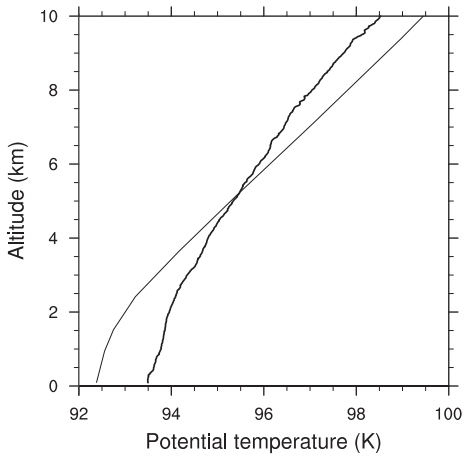

Fig. 19. Potential temperature vertical profile at 10°S (zonal average) and L_s = 300°, corresponding to the Huygens descent. The HASI/Huygens potential temperature profile is also shown (bold line).

et al. (2010). In Fig. 19, the diurnally averaged potential temperature profile in the GCM is shown for the deepest 10 km, at the Huygens landing site and season, together with the Huygens profile. The simulated boundary layer is located in the deepest 2 km, with an increase of 7 K between the surface and 10 km altitude. A detailed analysis of the diurnal and seasonal evolution of this near-surface potential temperature profile appears in a dedicated study (Charnay and Lebonnois, 2011). The modeled surface temperature at this point (and also its latitudinal profile) is sensitive to the choices of thermal inertia and albedo, and is also sensitive to the vertical distribution of haze. Clouds (not included here) may also affect the surface temperature.

The profiles of diurnally averaged zonal and meridional winds in the troposphere at the Huygens landing site have been retrieved from the probe's trajectory (Tokano, 2009, Fig. 2). These are shown together with the modeled wind profiles at the same location and season in Fig. 20. As seen in Fig. 9, the vertical profile of the zonal wind in the troposphere is in very good agreement with the measurements of the Huygens probe. Just above the surface, the wind is slightly positive (eastward), though it is mostly negative in the deepest 5 km, as in the observations. However, the amplitude of this westward wind is approximately half of the observed value. When reduced thermal inertia is used, the amplitude of wind variations are enhanced, and the retrograde region (negative u) persists up to 7–8 km.

The comparison between model and observations is less satisfactory for the meridional wind. Southward wind (negative) is indeed obtained just above the surface, but again the amplitude is only half the observed value. Between 1 and 5 km, both observed and modeled winds are northward, though modeled values are much less than observations. Above 3 km, the modeled meridional wind is almost zero up to the tropopause. The northward and southward winds present in the observations above 5 km are not obtained in the simulation. However, this observed profile corresponds to an instantaneous profile where waves and topographic effects may have been present.

Specific studies dedicated to the troposphere are underway and will be presented in future papers.

5. Conclusion

Based on the current version of the LMDZ Earth General Circulation Model dynamical core, we have developed a new model of Titan's atmosphere, including physic parametrizations from the IPSL 2-dimensional Titan Climate Model (2D-CM). However, due to computational limitations, microphysics of the haze and photochemistry are still computed as zonal averages. The new GCM simulation presented in this work has been initialized with the 2D-CM reference state at northern spring equinox and run for 12 Titan years.

Comparing this new simulation to previous 2-dimensional simulations and to observations, the following conclusions may be drawn:

- The modeled temperature structure is fairly similar between both models, with the same problems in the upper stratosphere where the temperatures are too cold, and above the 10 hPa level (approximately 300 km altitude) where no stratopause is obtained and the temperature is not realistic compared to observations. As in the 2D-CM, this is presumably related to the limitations of the radiative transfer and to the upper boundary position, which limits the altitude of the haze production region.

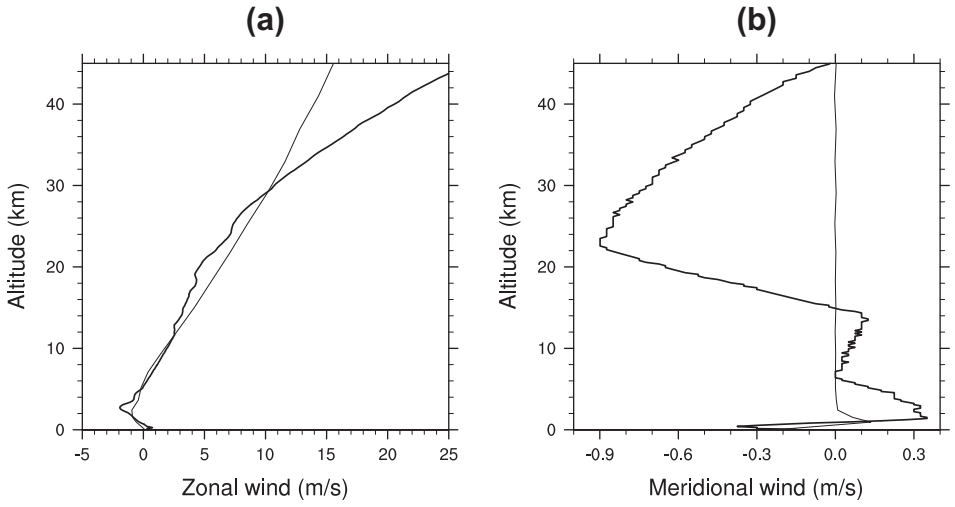

Fig. 20. Zonal (a) and meridional (b) wind vertical profiles at 10°S (zonal average) and L_s = 300°, corresponding to the Huygens descent. Values computed from the Huygens descent trajectory dataset (Tokano, 2009) are also plotted (bold lines).

- The comparison to observed latitudinal profiles of temperature in the lower stratosphere shows that the overall modeled temperature structure appears compressed in altitude. In spring, the comparison is not as good as for the 2D-CM, probably because of the haze distribution.
- The detached haze layer is present most of the year, lower than observed as in the 2D-CM. It shrinks and disappears after equinox, due to the shift of the ascending region from one pole to the other. The altitude difference between Cassini and Voyager 1 observations is a seasonal effect, now confirmed by the Cassini monitoring of the detached haze layer over the equinox (West et al., 2011). Comparing simulations with observations of this transition period should help to clarify the interaction between the haze and the atmospheric circulation.
- The zonal wind peak modeled at Cassini season is lower in amplitude as well as in altitude in this new simulation compared to the 2D-CM. However, the temporal evolution of the zonal wind field is qualitatively consistent with available observations.
- Changing the planetary boundary layer scheme has greatly improved agreement between the model and the tropospheric profile of the zonal wind from the Huygens descent.
- As in previous LMD models, a minimum in the zonal wind field is obtained close to the region where Huygens observed a stronger minimum in the equatorial lower stratosphere. In the simulation, this minimum is correlated with a local minimum in the temperature field, due to the relative distributions of solar forcing and dynamical transport of energy. According to the thermal wind equation, the observed wind minimum could correspond to an equatorial temperature around 2 K lower than mid-latitudes at 20–40 hPa (60–75 km altitude). This region is also correlated with a reversal (change of sign) of the meridional wind.
- In this 3D simulation, the diurnal cycle has been taken into account, but its role is minor. Barotropic instabilities, diagnosed and parameterized in the 2D-CM, are now explicitely simulated and many waves are visible in the stratosphere, mostly in the region around the zonal wind maximum. The horizontal transport of angular momentum by the mean meridional circulation is similar to the 2D simulation. However, the transport by transient waves is more complicated than in previous work. Barotropic waves transport momentum opposite to mean meridional circulation in mid- to low-latitudes, but a second component of the momentum transport appears at mid- to high-latitudes, due to low-frequency waves located close to the surface. Instability criterion as well as the more baroclinic characteristics of this region indicate that these waves are baroclinic waves. They transport momentum poleward at high latitudes all year long.
- In the lower troposphere, simulated potential temperature, zonal and meridional winds are compared to Huygens descent profiles. Though the amplitudes of wind variations are smaller than observed, the vertical profiles are very similar, except for the meridional wind above 3 km. Near-surface behavior of the model is sensitive to uncertain input parameters such as albedo and thermal inertia.

Due to the complex coupling between dynamics, haze particles and radiative transfer, it is difficult to adjust model parameters to get a circulation that fits observations everywhere. The model needs to be improved, especially above 300 km altitude where the temperature structure is far from observations. This affects the top of the haze layer as well as its time variability, and the resulting zonal wind structure and temperature distributions. The upgrade of the radiative transfer module in the GCM and the vertical extension of the upper boundary are underway and should help improve this situation.

Acknowledgements

The authors thank Frederic Hourdin for very useful discussions on the model and on this paper. This work has been supported by the project Exoclimats financed by the Agence Nationale de la Recherche (ANR), and by the computation facilities of both the Institut du Développement et des Ressources en Informatique Scientifique (IDRIS) and the University Pierre and Marie Curie (UPMC).

References

Achterberg, R.K., Conrath, B.J., Gierasch, P.J., Flasar, F.M., Nixon, C.A., 2008a. Observation of a tilt of Titan's middle-atmospheric superrotation. Icarus 197, 549–555.

Achterberg, R.K., Conrath, B.J., Gierasch, P.J., Flasar, F.M., Nixon, C.A., 2008b. Titan's middle-atmospheric temperatures and dynamics observed by the Cassini Composite Infrared Spectrometer. Icarus 194, 263–277.

Bird, M.K. et al., 2005. The vertical profile of winds on Titan. Nature 438, 1–3.

Bouchez, A., 2004. Seasonal Trends in Titan's Atmosphere: Haze, Winds, and Clouds. Ph.D. thesis. California Institute of Technology.

Charnay, B., Lebonnois, S., 2011. Thermal structure and dynamics of Titan's lower troposphere. Nat. Geosci., in press.
Coustenis, A., Bézard, B., 1995. Titan's atmosphere from Voyager infrared observations. IV. Latitudinal variations of temperature and composition. Icarus 115, 126–140.
Coustenis, A. et al., 2003. Titan's atmosphere from ISO mid-infrared spectroscopy. Icarus 161, 383–403.
Coustenis, A. et al., 2007. The composition of Titan's stratosphere from Cassini/CIRS mid-infrared spectra. Icarus 189, 35–62.
Coustenis, A., Jennings, D., Nixon, C., Achterberg, R.K., Lavvas, P., Vinatier, S., Teanby, N.A., Bjoraker, G.L., Carlson, R.C., Piani, L., Bampasidis, G., Flasar, F.M., Romani, P.N., 2010. Titan trace gaseous composition from CIRS at the end of the Cassini–Huygens prime mission. Icarus 207, 461–476.
Crespin, A., Lebonnois, S., Vinatier, S., Bézard, B., Coustenis, A., Teanby, N.A., Achterberg, R.K., Rannou, P., Hourdin, F., 2008. Diagnostics of Titan's stratospheric dynamics using Cassini/CIRS data and the IPSL General Circulation Model. Icarus 197, 556–571.
Del Genio, A.D., Zhou, W., Eichler, T.P., 1993. Equatorial superrotation in a slowly rotating GCM: Implications for Titan and Venus. Icarus 101, 1–17.
Flasar, F.M. et al., 2005. Titan's atmospheric temperatures, winds, and composition. Science 308, 975–978.
Flasar, F.M., Achterberg, R.K., 2009. The structure and dynamics of Titan's middle atmosphere. Philos. Trans. Roy. Soc. A 367, 649–664.
Flasar, F.M., Samuelson, R.E., Conrath, B.J., 1981. Titan's atmosphere: Temperature and dynamics. Nature 292, 693–698.
Folkner, W.M. et al., 2006. Winds on Titan from ground-based tracking of the Huygens probe. J. Geophys. Res. 111, E07S02.
Friedson, A.J., West, R.A., Wilson, E.H., Oyafuso, F., Orton, G.S., 2009. A global climate model of Titan's atmosphere and surface. Planet. Space Sci. 57, 1931–1949.
Fulchignoni, M. et al., 2005. In situ measurements of the physical characteristics of Titan's environment. Nature 438, 1–7.
Holton, J.R., 1992. An introduction to dynamic meteorology. In: International Geophysics Series, third ed. Academic Press, San Diego, New York.
Hourdin, F. et al., 2006. The LMDZ4 general circulation model: Climate performance and sensitivity to parameterized physics with emphasis on tropical convection. Clim. Dyn. 27, 787–813.
Hourdin, F., Le Van, P., Forget, F., Talagrand, O., 1993. Meteorological variability and the annual surface pressure cycle on Mars. J. Atmos. Sci. 50, 3625–3640.
Hourdin, F., Talagrand, O., Sadourny, R., Courtin, R., Gautier, D., McKay, C.P., 1995. Numerical simulation of the general circulation of the atmosphere of Titan. Icarus 117, 358–374.
Hourdin, F., Couvreux, F., Menut, L., 2002. Parameterization of the dry convective boundary layer based on a mass flux representation of thermals. J. Atmos. Sci. 59, 1105–1123.
Hourdin, F., Lebonnois, S., Luz, D., Rannou, P., 2004. Titan's stratospheric composition driven by condensation and dynamics. J. Geophys. Res. 109, E12005.
Hubbard, W.B. et al., 1993. The occultation of 28 Sgr by Titan. Astron. Astrophys. 269, 541–563.
Jennings, D.E. et al., 2009. Titan's surface brightness temperatures. Astrophys. J. 691, L103–L105.
Kostiuk, T. et al., 2001. Direct measurements of winds on Titan. Geophys. Res. Lett. 28, 2361–2364.
Kostiuk, T. et al., 2005. Titan's stratospheric zonal wind, temperature, and ethane abundance a year prior to Huygens insertion. Geophys. Res. Lett. 32, L22205.
Kostiuk, T. et al., 2006. Stratospheric global winds on Titan at the time of Huygens descent. J. Geophys. Res. 111, E07S03.
Kostiuk, T. et al., 2010. High spectral resolution infrared studies of Titan: Winds, temperature, and composition. Planet. Space Sci. 58, 1715–1723.
Kuo, H.I., 1949. Dynamic instability of 2-dimensional nondivergent flow in a barotropic atmosphere. J. Meteor. 6, 105–122.
Lebonnois, S., Toublanc, D., Hourdin, F., Rannou, P., 2001. Seasonal variations in Titan's atmospheric composition. Icarus 152, 384–406.
Lebonnois, S., Hourdin, F., Rannou, P., Luz, D., Toublanc, D., 2003. Impact of the seasonal variations of ethane and acetylene distributions on the temperature field of Titan's stratosphere. Icarus 163, 164–174.
Lebonnois, S., Hourdin, F., Rannou, P., 2009. The coupling of winds, aerosols and photochemistry in Titan's atmosphere. Philos. Trans. Roy. Soc. A 367, 665–682.
Lebonnois, S., Hourdin, F., Eymet, V., Crespin, A., Fournier, R., Forget, F., 2010. Superrotation of Venus' atmosphere analysed with a full General Circulation Model. J. Geophys. Res. 115, E06006.
Lebonnois, S. et al., 2011. A comparative analysis of simplified general circulation models of Venus atmosphere. In: Towards Understanding the Climate of Venus: Application of Terrestrial Models to Our Sister Planet. Springer, Netherlands, in press.
Lebreton, J.P., Coustenis, A., Lunine, J., Raulin, F., Owen, T., Strobel, D., 2009. Results from the Huygens probe on Titan. Astron. Astrophys. Rev. 17, 149–179.
Lorenz, R.D., Claudin, P., Andreotti, B., Radebaugh, J., Tokano, T., 2010. A 3 km atmospheric boundary layer on Titan indicated by dune spacing and Huygens data. Icarus 205, 719–721.
Luz, D., Hourdin, F., 2003. Latitudinal transport by barotropic waves in Titan's stratosphere. I. General properties from a horizontal shallow-water model. Icarus 166, 328–342.
Luz, D., Hourdin, F., Rannou, P., Lebonnois, S., 2003. Latitudinal transport by barotropic waves in Titan's stratosphere. II. Results from a coupled dynamics–microphysics–photochemistry GCM. Icarus 166, 343–358.
Luz, D., Civeit, T.R.C., Lebreton, J.P., Gautier, D., Rannou, P., Kaufer, A., Witasse, O., Lara, L., Ferri, F., 2005. Characterization of zonal winds in the stratosphere of Titan with UVES. Icarus 179, 497–510.
Marten, A., Hidayat, T., Biraud, Y., Moreno, R., 2002. New millimeter heterodyne observations of Titan: Vertical distributions of nitriles HCN, HC_3N, CH_3CN, and the isotopic ratio $^{15}N/^{14}N$ in its atmosphere. Icarus 158, 532–544.
McKay, C.P., Pollack, J.B., Courtin, R., 1989. The thermal structure of Titan's atmosphere. Icarus 80, 23–53.
Mellor, G.L., Yamada, T., 1982. Development of a turbulent closure model for geophysical fluid problems. Rev. Geophys. Space Phys. 20, 851–875.
Mingalev, I.V. et al., 2006. First simulation results of Titan's atmospheric dynamics with a global 3-D non-hydrostatic circulation model. Ann. Geophys. 24, 1–15.
Mitchell, J.L., Vallis, G.K., 2010. The transition to superrotation in terrestrial atmospheres. J. Geophys. Res. 115, E12008.
Mitchell, J.L., Pierrehumbert, R.T., Frierson, D., Caballero, R., 2006. The dynamics behind Titan's methane cloud. Proc. Nat. Acad. Sci. 103, 18421–18426.
Mitchell, J.L., Ádámkovics, M., Caballero, R., Turtle, E.P., 2011. Locally enhanced precipitation organized by planetary-scale waves on Titan. Nat. Geosci. 4, 589–592.
Moreno, R., Marten, A., Hidayat, T., 2005. Interferometric measurements of zonal winds on Titan. Astron. Astrophys. 437, 319–328.
Newman, C.E., Lee, C., Lian, Y., Richardson, M.I., Toigo, A.D., 2011. Stratospheric superrotation in the TitanWRF model. Icarus 213, 636–654.
Niemann, H.B. et al., 2005. The abundances of constituents of Titan's atmosphere from the GCMS instrument on the Huygens probe. Nature 438, 1–6.
Rannou, P., Hourdin, F., McKay, C.P., 2002. A wind origin for Titan's haze structure. Nature 418, 853–856.
Rannou, P., Hourdin, F., McKay, C.P., Luz, D., 2004. A coupled dynamics-microphysics model of Titan's atmosphere. Icarus 170, 443–462.
Rannou, P., Lebonnois, S., Hourdin, F., Luz, D., 2005. Titan atmosphere database. Adv. Space Res. 36, 2194–2198.
Rannou, P., Montmessin, F., Hourdin, F., Lebonnois, S., 2006. The latitudinal distribution of clouds on Titan. Science 311, 201–205.
Richardson, M.I., Toigo, A.D., Newman, C.E., 2007. PlanetWRF: A general purpose, local to global numerical model for planetary atmospheric and climate dynamics. J. Geophys. Res. 112, E09001.
Schinder, P.J., Flasar, F.M., Marouf, E.A., French, R.G., McGhee, C.A., Kliore, A.J., Rappaport, N.J., Barbinis, E., Fleischman, D., Anabtawi, A., 2011. The structure of Titan's atmosphere from Cassini radio occultations. Icarus 215, 460–474.
Sicardy, B. et al., 2006. The two Titan stellar occultations of 14 November 2003. J. Geophys. Res. 111, E11S91.
Teanby, N.A. et al., 2008a. Titan's winter polar vortex structure revealed by chemical tracers. J. Geophys. Res. 113, E12003.
Teanby, N.A., Irwin, P.G.J., de Kok, R., Nixon, C.A., Coustenis, A., Bézard, B., Calcutt, S.B., Bowles, N.E., Flasar, F.M., Fletcher, L., Howett, C., Taylor, F.W., 2006. Latitudinal variations of HCN, HC_3N and C_2N_2 in Titan's stratosphere derived from Cassini CIRS data. Icarus 181, 243–255.
Teanby, N.A., Irwin, P.G.J., de Kok, R., Vinatier, S., Bézard, B., Nixon, C.A., Flasar, F.M., Calcutt, S.B., Bowles, N.E., Fletcher, L., Howett, C., Taylor, F.W., 2007. Vertical profiles of HCN, HC_3N and C_2H_2 in Titan's atmosphere derived from Cassini/CIRS data. Icarus 186, 364–384.
Teanby, N.A., Irwin, P.G.J., de Kok, R., Nixon, C.A., Coustenis, A., Royer, E., Calcutt, S.B., Bowles, N.E., Fletcher, L., Howett, C., Taylor, F.W., 2008b. Global and temporal variations in hydrocarbons and nitriles in Titan's stratosphere for northern winter observed by Cassini/CIRS. Icarus 193, 595–611.
Teanby, N.A., Irwin, P.G.J., de Kok, R., Jolly, A., Bézard, B., Nixon, C.A., Calcutt, S.B., 2009a. Titan's stratospheric C_2N_2, C_3H_4 and C_4H_2 abundances from Cassini/CIRS far-infrared spectra. Icarus 202, 620–631.
Teanby, N.A., Irwin, P.G.J., de Kok, R., Nixon, C.A., 2009b. Dynamical implications of seasonal and spatial variations in Titan's stratospheric composition. Philos. Trans. Roy. Soc. A 367, 697–711.
Tokano, T., 2009. The dynamics of Titan's troposphere. Philos. Trans. Roy. Soc. A 367, 633–648.
Tokano, T., Neubauer, F.M., Laube, M., McKay, C.P., 1999. Seasonal variation of Titan's atmospheric structure simulated by a general circulation model. Planet. Space Sci. 47, 493–520.
Tokano, T., Ferri, F., Colombatti, G., Mäkinen, T., Fulchignoni, M., 2006. Titan's planetary boundary layer structure at the Huygens landing site. J. Geophys. Res. 111, E08007.
Tomasko, M.G. et al., 2005. Rain, winds and haze during the Huygens probe's descent to Titan's surface. Nature 438, 1–14.
Turtle, E.P. et al., 2011. Seasonal changes in Titan's meteorology. Geophys. Res. Lett. 38, L03203.
Vallis, G.K., 2006. Atmospheric and Oceanic Fluid Dynamics. Cambridge University Press, Cambridge, UK.
Vinatier, S., Bézard, B., Fouchet, T., Teanby, N.A., de Kok, R., Irwin, P., Conrath, B.J., Nixon, C.A., Romani, P.N., Flasar, F.M., Coustenis, A., 2007. Vertical abundance profiles of hydrocarbons in Titan's atmosphere at 15°S and 80°N retrieved from Cassini/CIRS spectra. Icarus 188, 120–138.
Vinatier, S., Bézard, B., Nixon, C.A., Mamoutkine, A., Carlson, R.C., Jennings, E.D., Guandique, E.A., Teanby, N.A., Bjoraker, G.L., Flasar, F.M., Kunde, V.G., 2010. Analysis of Cassini/CIRS spectra of Titan acquired during the nominal mission. I. Hydrocarbons, nitriles and CO_2 vertical mixing ratio profiles. Icarus 205, 559–570.
West, R.A. et al., 2011. The evolution of Titan's detached haze layer near equinox in 2009. Geophys. Res. Lett. 380, L06204.